

#### **TOPICAL REVIEW**

## On Co<sub>3</sub>Sn<sub>2</sub>S<sub>2</sub> surfaces: crystal growth, surface recognition, atomic engineering and novel quantum structures

To cite this article: Li Huang et al 2025 J. Phys.: Condens. Matter 37 473005

View the article online for updates and enhancements.

#### You may also like

- Whither nanomaterials? Thomas E Mallouk, Fred Pinkerton and Ned Stetson
- Foreword
- Bonding-Driven Crystallization of Dimensionally Resolved Nanostructures Based on Quasi-1D Van Der Waals Building Blocks

Maxx Arguilla, Dmitri Leo Mesoza Cordova and Steven Jay Allison

#### **Topical Review**

# On Co<sub>3</sub>Sn<sub>2</sub>S<sub>2</sub> surfaces: crystal growth, surface recognition, atomic engineering and novel quantum structures

Li Huang<sup>1,2</sup>, Yuqing Xing<sup>1,2</sup>, Qi Zheng<sup>1,2</sup>, Senhao Lv<sup>1,2</sup>, Lan Chen<sup>1,2</sup>, Hui Chen<sup>1,2</sup>, Haitao Yang<sup>1,2</sup>, Wei Ji<sup>3</sup> and Hong-Jun Gao<sup>1,2,\*</sup>

E-mail: hjgao@iphy.ac.cn

Received 18 September 2025, revised 3 November 2025 Accepted for publication 11 November 2025 Published 20 November 2025



#### Abstract

Kagome-lattice magnetic Weyl semimetal Co<sub>3</sub>Sn<sub>2</sub>S<sub>2</sub> has emerged as a versatile platform for exploring interplays among band topology, magnetism, and electron correlations, exhibiting potentials for next-generation electronic and spintronic applications. This review provides an overview of recent advances in understanding the surface atomic and electronic structures and discovering novel physical properties of this material. We first present the synthesis of ultra-high quality Co<sub>3</sub>Sn<sub>2</sub>S<sub>2</sub> single crystals by iterative chemical vapor transport growth methodology, which enables the growth of large, stoichiometric crystals with significantly enhanced physical properties. Next, we elucidate atomic scale identification of cleaved surfaces using joint work function measurements, bond-resolved non-contact atomic force microscopy, short-range force spectroscopy, and density functional theory calculations. Based on the explicitly identified surface, we next highlight the discovery and manipulation of localized spin-orbit polarons (SOPs) at S vacancies on the S surface, emphasizing their electronic and magnetic properties and the ability of manipulating specific SOP configurations at the atomic scale. We further show oxygen-induced quantum clusters, where O dopants modify the electronic states of surrounding atoms, providing building blocks for scalable functional quantum structures. Finally, we present the discovery of kagome electronic states on the Sn-terminated triangular-lattice surface and outline a proposed strategy for constructing such states with tunable properties. Collectively, these developments illustrate how high-quality crystal growth, atomic-scale imaging and manipulation, and defect/dopant engineering can be effectively integrated to discover and manipulate emergent novel physical properties of a kagome Weyl semimetal, opening new avenues for atomically precise design and surface state engineering in quantum materials.

<sup>&</sup>lt;sup>1</sup> Beijing National Center for Condensed Matter Physics and Institute of Physics, Chinese Academy of Sciences, Beijing 100190, People's Republic of China

<sup>&</sup>lt;sup>2</sup> School of Physical Sciences, University of Chinese Academy of Sciences, Beijing 100190, People's Republic of China

<sup>&</sup>lt;sup>3</sup> Beijing Key Laboratory of Optoelectronic Functional Materials & Micro-Nano Devices, Department of Physics, Renmin University of China, Beijing 100872, People's Republic of China

<sup>\*</sup> Author to whom any correspondence should be addressed.

Keywords: kagome Weyl magnet, Co<sub>3</sub>Sn<sub>2</sub>S<sub>2</sub>, scanning tunneling microscopy, qPlus non-contact atomic force microscopy, atomic manipulation, density functional theory

#### 1. Introduction

Kagome-lattice materials have emerged as a fertile platform for investigating unconventional quantum states arising from the interplay of lattice geometry, strong electron correlations, magnetism, and nontrivial band topology [1-10]. The kagome network, comprised of corner-sharing triangles, gives rise to a distinctive electronic structure characterized by Dirac cones, flat bands, and van Hove singularities, which can give rise to a wide spectrum of exotic phases, including exotic electronic states such as quantum spin liquids, charge density waves, and topological states, as well as unconventional superconductivity [11-46]. Among kagome materials, magnetic Weyl semimetals [8, 47-51] have attracted particular attention due to their strong spin-orbit coupling (SOC) and nontrivial Berry curvature, which give rise to a large anomalous Hall effect (AHE) even at room temperature, as observed in the ferromagnet Fe<sub>3</sub>Sn<sub>2</sub> [52] and the antiferromagnet Mn<sub>3</sub>Sn [53]. Co<sub>3</sub>Sn<sub>2</sub>S<sub>2</sub>, containing kagome lattices of Co atoms within in Co<sub>3</sub>Sn planes, is the first Weyl semimetal experimentally confirmed to host characteristic bulk Weyl points with linear dispersions and surface Fermi arcs [54]. Extensive studies on Co<sub>3</sub>Sn<sub>2</sub>S<sub>2</sub> have revealed a variety of remarkable phenomena [54-66], including giant anomalous Hall/Nernst effect [55–57, 67, 68], chiral-anomaly [55], flat band and orbital magnetization [59], surface-terminationdependent Fermi arcs [60], and defect-induced tunability of electronic properties [69]. These features establish Co<sub>3</sub>Sn<sub>2</sub>S<sub>2</sub> as a prototypical platform for exploring emergent quantum phenomena in kagome magnets.

Figure 1 highlights the main progress in previous Co<sub>3</sub>Sn<sub>2</sub>S<sub>2</sub> investigations. Bulk Co<sub>3</sub>Sn<sub>2</sub>S<sub>2</sub> (figure 1(a)) adopts a rhombohedral crystal structure with space group  $R3\bar{m}$ , in which each kagome Co<sub>3</sub>Sn layer is sandwiched by two triangular S layers and these trilayers are further separated by triangular Sn layers. The presence of Weyl points of opposite chirality just above the Fermi level, accompanied by gapped nodal lines, identifies Co<sub>3</sub>Sn<sub>2</sub>S<sub>2</sub> as a topologically nontrivial material, with strong SOC playing a central role (figures 1(b) and (c)) [54, 55]. The Berry curvature hotspots associated with the Weyl nodes generate a giant intrinsic AHE, reflected by the large anomalous Hall conductivity and Hall angle measured experimentally [55] (figure 1(d)). In addition, the Weyl topological band structure in this magnetic system gives rise to distinctive surface states, including open Fermi arcs and topological edge modes, which have been directly visualized by surface-sensitive probes such as scanning tunneling microscopy (STM). The quasiparticle interference (QPI) technique was used to reveal surface-dependent scattering features in momentum space (figures 1(e) and (f)). In these measurements, Fermi-arc segments appear as linear features along  $\Gamma$ -M, forming a honeycomb-like pattern around the Bragg peaks in figure 1(f). These patterns reveal topological surface states (TSSs) linked bulk Weyl points, providing a direct visualization of the surface-bulk correspondence in this magnetic Weyl semimetal [60]. Topological nontrivial electronic transport and scattering properties aside, electrons filled in the nearly flat bands, intrinsic to the Co<sub>3</sub>Sn<sub>2</sub>S<sub>2</sub> kagome lattice, exhibit unusual correlation effects such as negative orbital magnetism under external magnetic fields (figure 1(g)) [59]. Moreover, linearly dispersing bound states have been observed on narrow Co<sub>3</sub>Sn terraces, demonstrating that time-reversal symmetry-breaking Weyl semimetals can host robust chiral edge states localized on exposed kagome planes (figure 1(h)) [62].

This review focuses on recent advances in the use of STM and non-contact atomic force microscopy (nc-AFM) to directly image and manipulate the atomic, electronic, and magnetic states in Co<sub>3</sub>Sn<sub>2</sub>S<sub>2</sub> Surfaces. It covers crystal growth, cleaved surface identification, and the discovery and manipulation of defect/dopants-induced unconventional quantum states. The review is organized in five parts as follows: (1) growth and physical properties of ultra-high-quality Co<sub>3</sub>Sn<sub>2</sub>S<sub>2</sub> single crystals [71]; (2) identification of cleaved surfaces with conclusive evidence [70]; (3) spin—orbit polaron (SOP) formation and atomic manipulation on the S surface [72, 73]; (4) oxygen-induced quantum clusters with tunable localized electronic states [74]; (5) Kagome electronic states discovered on triangular-lattice S and Sn surfaces [70].

## 2. Growth and physical properties of ultra-high-quality Co<sub>3</sub>Sn<sub>2</sub>S<sub>2</sub> single crystals

Considerable efforts have been devoted to achieving ultrahigh-quality  $Co_3Sn_2S_2$  samples, as they are essential for accurate measurements of fundamental properties such as electronic transport, magnetism, and topological states, and for providing a platform to tune and optimize these properties toward future applications.

## 2.1. Growth of ultra-high-quality $Co_3Sn_2S_2$ single crystals by iterative-chemical vapor transport (CVT) approach

Ultra-high-quality Co<sub>3</sub>Sn<sub>2</sub>S<sub>2</sub> single crystals have been obtained using an iterative CVT growth technique (figure 2) [71]. In this method, pre-grown Co<sub>3</sub>Sn<sub>2</sub>S<sub>2</sub> crystals serve as source materials instead of raw elements, which allows for better stoichiometry control, fewer defects and impurities, and the growth of larger and higher quality crystals. The iterative crystal-to-crystal growth with NH<sub>4</sub>Cl as the transport agent produces single crystals with well-defined hexagonal morphology and large lateral dimensions of millimeters (figure 3(a)), indicative of preferential growth along

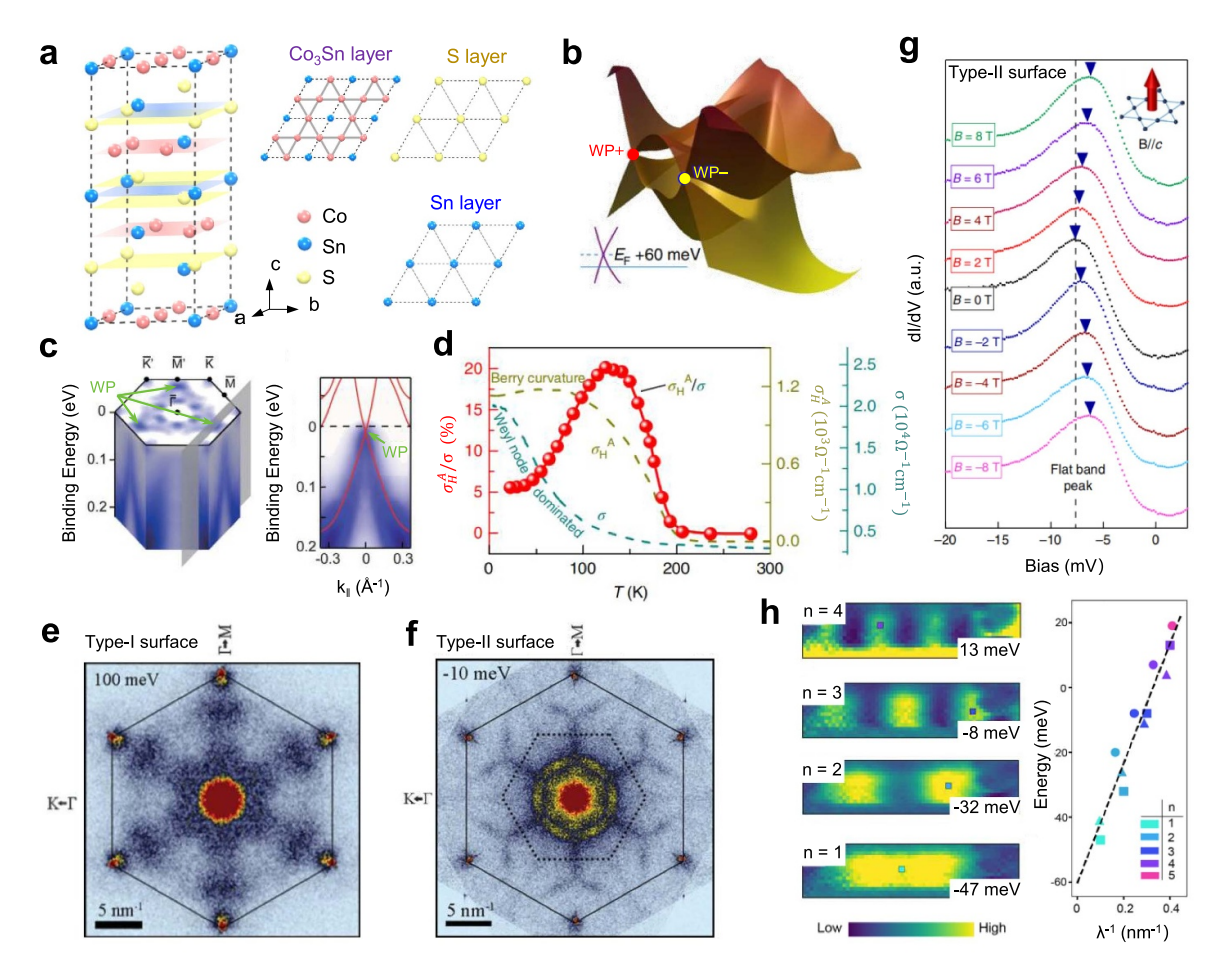


Figure 1. Geometric and electronic properties of Co<sub>3</sub>Sn<sub>2</sub>S<sub>2</sub>. (a) Atomic structures of Co<sub>3</sub>Sn<sub>2</sub>S<sub>2</sub>. Left: atomic structure of bulk, with the Sn, S and Co<sub>3</sub>Sn layers denoted by blue, yellow and red planes, respectively. Right: Atomic arrangements of the three atomic layers highlighted in the Left panel. Reproduced from [70]. CC BY 4.0. (b) Theoretically calculated band structure of Co<sub>3</sub>Sn<sub>2</sub>S<sub>2</sub> near the Fermi level, showing two Weyl points with different forms of chirality (denoted by WP±) residing 60 meV above the Fermi level. Reproduced from [55], with permission from Springer Nature. (c) Angle-resolved photoemission spectroscopy (ARPES) of Co<sub>3</sub>Sn<sub>2</sub>S<sub>2</sub>. Left: 3D ARPES intensity map acquired after potassium doping. The doping raises the Fermi level and thereby enables the observation of emergent Weyl points (indicated by green arrows). Right: experimental band structures along a cut through the Weyl point (grey plane in the left panel), showing two linearly dispersing bands crossing at the Weyl point, consistent with the theoretical results (red curves). From [54]. Reprinted with permission from AAAS. (d) Temperature dependence of the anomalous Hall angle ( $\sigma_{\rm H}^{\rm A}/\sigma$ , red dots), the anomalous Hall conductivity ( $\sigma_{\rm H}^{\rm A}$ , olive green dashed line), and the charge conductivity ( $\sigma$ ) at zero magnetic field. Reproduced from [55], with permission from Springer Nature. (e) Fourier-transformed dI/dV map acquired near the Weyl node energy (E = 100 mV) on the Type-I surface, exhibiting a flower-shaped quasiparticle interference (QPI) pattern around  $\Gamma$  and broad features along the  $\Gamma$ -M direction. (f) Fourier-transformed dI/dV map obtained at -10 mV on the Type-II surface, showing sharp QPI patterns. Scattering processes within the Brillouin zone (BZ) are enclosed by the dotted hexagon, while inter-BZ scattering is indicated by the solid hexagon connecting six Bragg peaks. From [60]. Reprinted with permission from AAAS. (g) Magnetic-field dependence of the flat band peak on the Type-II surface, which exhibits negative orbital magnetism. The inset illustrates the applied magnetic field oriented perpendicular to the kagome lattice. Reproduced from [59], with permission from Springer Nature. (h) Observation of linearly dispersing bound states on a Co<sub>3</sub>Sn kagome terrace. Reproduced from [62]. CC BY 4.0. Left: density of state maps at energies for each quantum-well-like state. Right: relation of energy versus inverse wavelength for states found on three Co<sub>3</sub>Sn terraces. The linear dashed line is provided as a guide to the eye..

the *ab* plane in alignment with the Co<sub>3</sub>Sn kagome lattice. By comparison, crystals grown by the conventional self-flux method are generally irregular and smaller, with lateral sizes of approximately 1–3 mm.

Co<sub>3</sub>Sn<sub>2</sub>S<sub>2</sub> single crystals synthesized via the iterative CVT method exhibit the excellent phase purity, near-ideal stoichiometry, and superior crystallinity. These qualities are evidenced by sharp x-ray diffraction (XRD) peaks,

narrow rocking curve widths, and well-defined diffraction spots (figure 3(b)). Atomic resolution scanning transmission electron microscopy (STEM) imaging along multiple crystallographic directions reveals a well-ordered hexagonal lattice and a clear spatial distribution of Co, Sn, and S atoms. Figure 3(c) displays the high-angle annular dark-field (HAADF) STEM image along the [001] zone axis, overlaid with the structural model and indexed Co<sub>3</sub>Sn kagome plane,

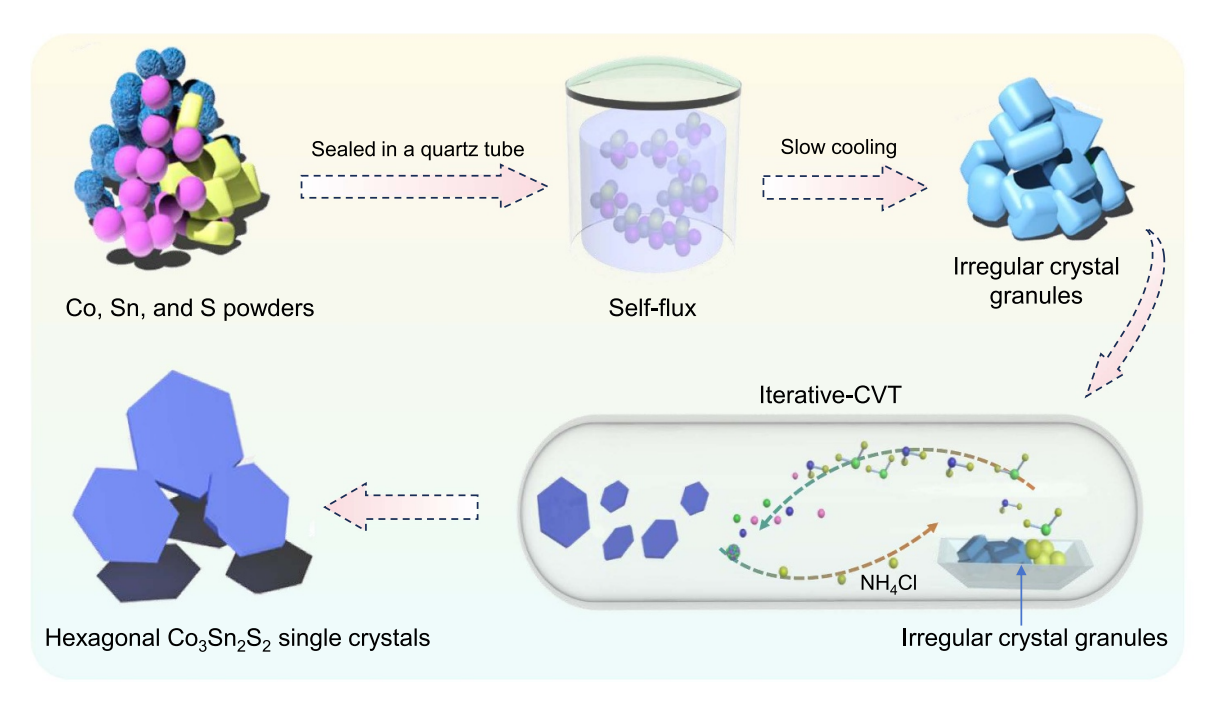


Figure 2. Synthesis of  $Co_3Sn_2S_2$  single crystals by iterative-CVT approach. Schematic illustration of the iterative-CVT growth procedure. The  $Co_3Sn_2S_2$  crystal granules, synthesized by the self-flux method, are placed in the high-temperature zone with NH<sub>4</sub>Cl as the transport agent. Large-size, hexagonal-shaped  $Co_3Sn_2S_2$  single crystals are collected in the low-temperature zone [71]. John Wiley & Sons. {@ original copyright notice}.

highlighting the well-ordered *ab*-plane with hexagonal symmetry. Figure 3(d) presents the HAADF image along the [100] zone axis, together with the corresponding structural models and indexed planes. Atomic resolution elemental mapping (figure 3(e)) further confirms the distinct distributions of Co, Sn, and S. Complementary XRD and STM measurements corroborate the high crystallinity and low defect density of crystals obtained by the iterative method, with STM images revealing a significantly lower impurity density compared to self-flux grown samples. These results collectively demonstrate that the iterative CVT approach yields Co<sub>3</sub>Sn<sub>2</sub>S<sub>2</sub> single crystals with markedly improved the structural quality and reduced impurity levels relative to those grown by conventional methods.

The iterative-CVT method produces significantly higherquality Co<sub>3</sub>Sn<sub>2</sub>S<sub>2</sub> single crystals than the conventional selfflux method, primarily due to three key advantages. First, using Co<sub>3</sub>Sn<sub>2</sub>S<sub>2</sub> crystal granules as precursors prevents unwanted reactions between Sn halides and the quartz tube, while maintaining optimal precursor concentration and growth rate to ensure precise Co, Sn, and S stoichiometry. Second, the use of non-volatile NH<sub>4</sub>Cl maintains a high vacuum level  $(4 \times 10^{-5} \text{ Pa})$  and a stable growth temperature, creating a clean, controlled environment that promotes preferential growth along the (001) planes while preventing contamination from flux residues and trapped air. Third, NH<sub>4</sub>Cl, with its higher electronegativity compared to I2, enhances the transport rate, increasing precursor feedstock concentration in the growth zone [75] and enabling the synthesis of larger, higherquality Co<sub>3</sub>Sn<sub>2</sub>S<sub>2</sub> single crystals.

## 2.2. Electronic properties of the ultra-high-quality $Co_3Sn_2S_2$ single crystals

High-resolution vacuum ultraviolet laser angle-resolved photoemission spectroscopy (ARPES) [76] has provided valuable insights into the electronic structure of ultra-high-quality Co<sub>3</sub>Sn<sub>2</sub>S<sub>2</sub> single crystals. Fermi surface mapping reveals six small pockets around the Brillouin zone (BZ) center  $\Gamma$ , in excellent agreement with DFT calculations (figures 4(a) and (b)). Along the  $\Gamma$ -K direction, TSSs have been clearly identified about 0.4 Å<sup>-1</sup> from the K point (figure 4(c)), consistent with theoretical predictions and previous reports. In addition, ARPES measurements along orthogonal momentum cuts show an isolated, nearly dispersionless flat band near the K point (figures 4(d) and (e)), characterized by a narrow intrinsic linewidth close to the thermal broadening limit. This observation agrees well with DFT calculations (figure 4(f)) and represents one of the clearest visualizations of a flat band in a ferromagnetic kagome semimetal. The presence of such an ultra-narrow flat band, which is generally unexpected for kagome d-orbitals due to symmetry and crystal field effects [77], highlights the importance of exceptional crystal quality and suggests a promising platform for exploring strongly correlated phenomena, such as orbital diamagnetism.

The enhanced crystal quality also leads to substantial improvements in key electrical transport properties. It has a ferromagnetic transition at a Curie temperature of 177 K. The residual resistivity ratio (RRR =  $\rho_{300 \text{ K}}/\rho_{2 \text{ K}}$ ) exceeds 128, and the conductivity reaches 2.3  $\times$  10<sup>5</sup>  $\Omega^{-1}$  · cm<sup>-1</sup>

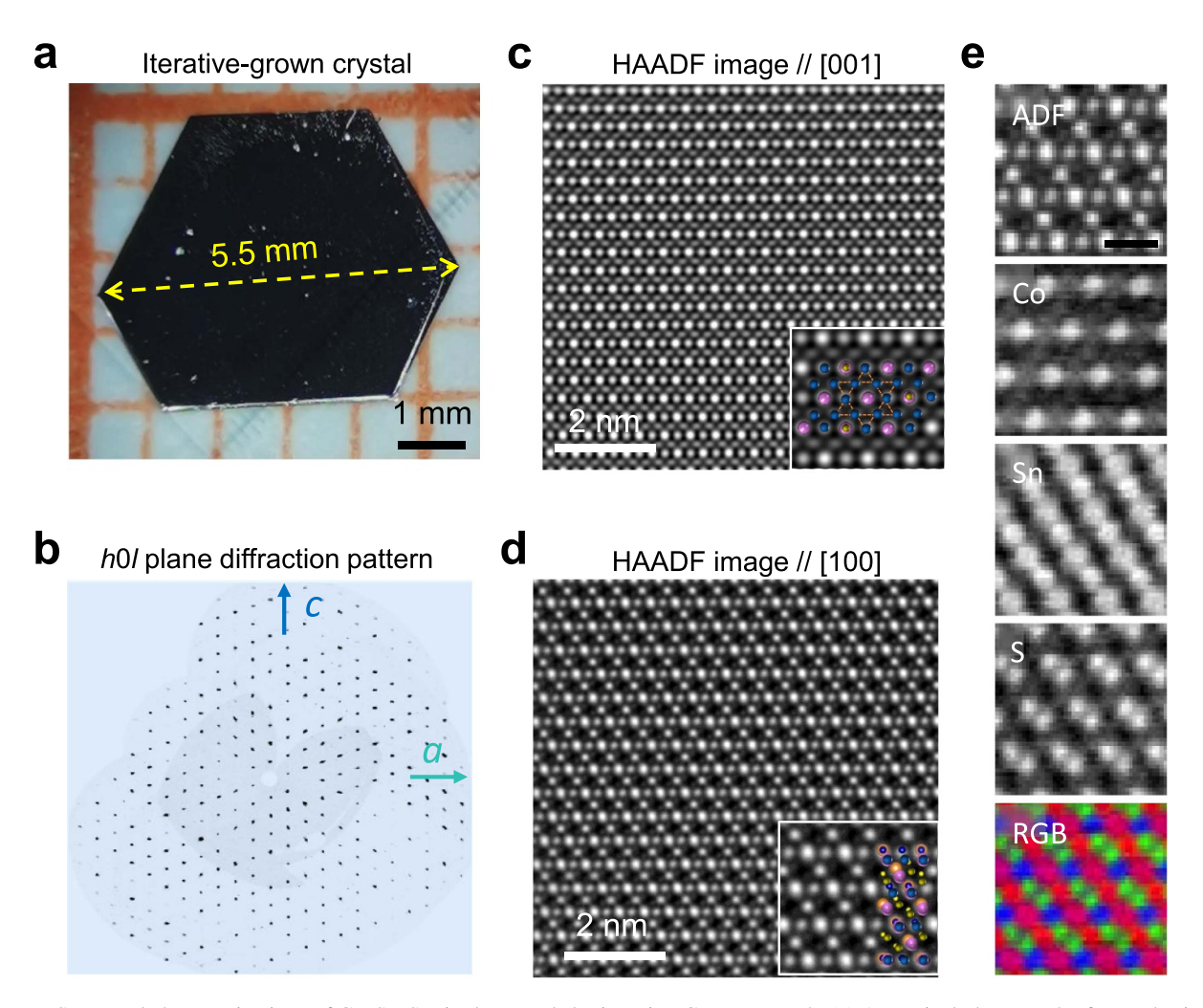


Figure 3. Structural characterizations of  $Co_3Sn_2S_2$  single crystals by iterative-CVT approach. (a) An optical photograph of a synthesized hexagonal-shaped  $Co_3Sn_2S_2$  single crystal via the iterative-CVT approach, showing the lateral size of about 5.5 mm. (b) h0l plane diffraction patterns of the  $Co_3Sn_2S_2$  single crystals prepared by the iterative-CVT method, showing sharp diffraction spots without splitting. (c,d) High-resolution HAADF STEM images along the [001] and [100] axis of the iterative-grown  $Co_3Sn_2S_2$  single crystal, respectively. The insets are close-up images with overlayed atomic model, where blue, pink, and yellow balls represent the Co, Sn and S atoms, respectively. (e) Electron energy loss spectroscopy (EELS) elemental mapping of the Co–L, Sn–M and S–L edges, showing the elemental distributions. The RGB false-color map highlights the spatial distribution of Co (blue), Sn (red), S (green) elements [71]. John Wiley & Sons. {@ original copyright notice}.

at 2 K, both roughly an order of magnitude higher than the reported values on crystals grown by the conventional selfflux method [55, 56]. Magneto-transport measurements under out-of-plane magnetic fields reveal a non-saturating positive magnetoresistance (MR) of up to 2500% at 2 K, far exceeding previously reported values of 55%-250% [55, 68]. Furthermore, an in-plane negative MR and a planar Hall effect are observed, consistent with the chiral anomaly associated with Weyl fermions. By fitting the transverse and longitudinal conductivity using the semiclassical Drude model, the extracted carrier densities at 2 K are approximately 7.9  $\times$  10<sup>19</sup> cm<sup>-3</sup> for electrons and 2.2  $\times$  10<sup>20</sup> cm<sup>-3</sup> for holes, indicating bipolar transport. The corresponding carrier mobilities are 10 490  $\pm$  45 cm<sup>2</sup>  $\cdot$  V<sup>-1</sup>  $\cdot$  s<sup>-1</sup> for electrons and 2504  $\pm$  8 cm<sup>2</sup> · V<sup>-1</sup> · s<sup>-1</sup> for holes, surpassing those of most known magnetic topological semimetals.

## 2.3. Enhanced AHE observed on the ultra-high-quality $Co_3Sn_2S_2$ single crystals

The AHE is further examined through magnetic-field-dependent Hall resistivity  $(\rho_{yx})$  measurements at various temperatures. The results show a combination of AHE with hysteresis and a nonlinear normal Hall response, indicating a two-carrier conduction mechanism. The total Hall conductivity  $(\sigma_{yx})$  measured at 2 K and 50 K (figure 5(a)) reveals a pronounced anomalous Hall conductivity  $(\sigma_{yx}^{A})$  with strong temperature dependence (figure 5(b)). Notably,  $\sigma_{yx}^{A}$  increases from 980  $\Omega^{-1} \cdot \text{cm}^{-1}$  at 2 K to reach a maximum value of  $\sim 1600 \Omega^{-1} \cdot \text{cm}^{-1}$  at 50 K, representing a  $\sim 65\%$  enhancement that deviates from previously reported data [55]. Furthermore, the anomalous Hall angle (AHA,  $\sigma_{yx}^{A}/\sigma_{xx}$ ) exceeds 30% across a wide temperature range of 100–160 K and peaks at  $\sim 40\%$  around 140 K (figure 5(c)),

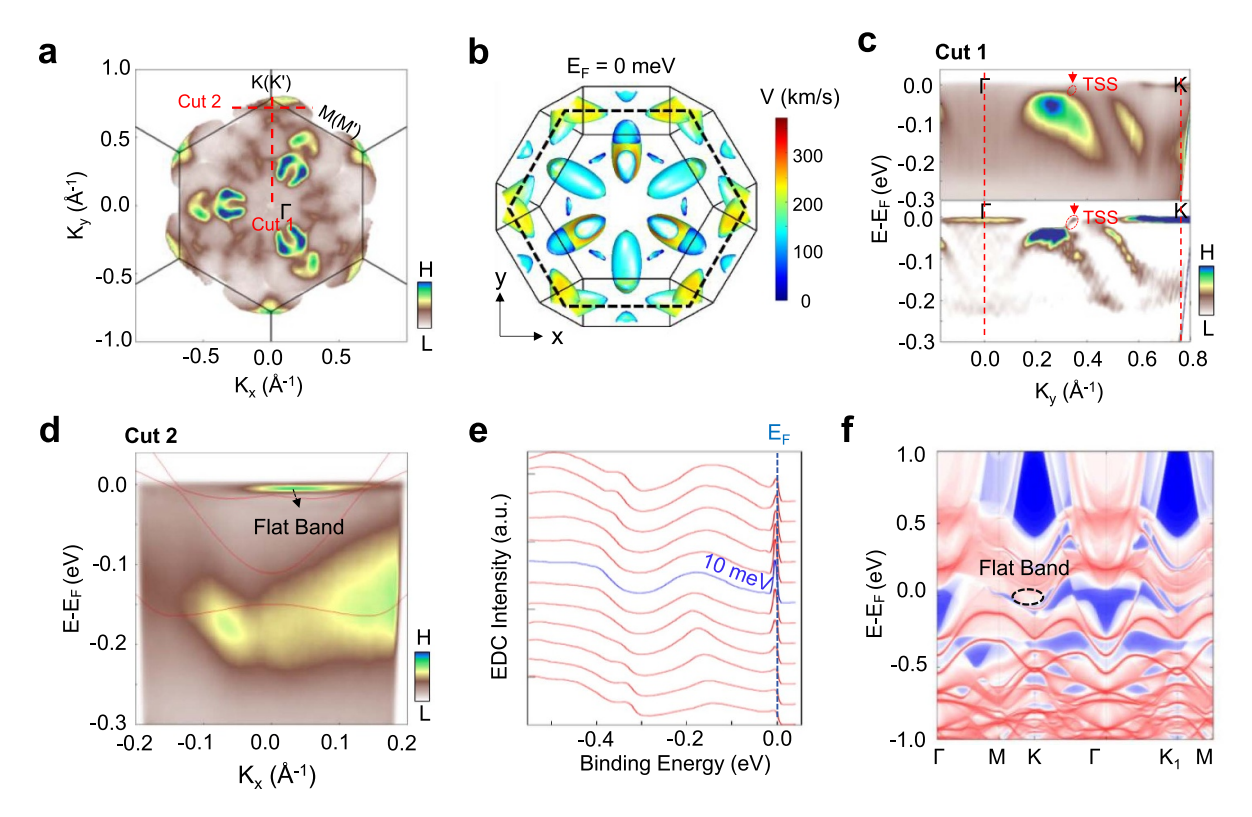


Figure 4. Visualization of ultranarrow kagome flat band and TSS around the Fermi level. (a) Fermi surface mapping integrated within  $\pm$  10 meV. The red dotted lines along  $K_y$  and  $K_x$  are marked as Cut 1 and Cut 2 for band measurements in (c) and (d), respectively. (b) DFT-calculated Fermi surface projections showing good agreement with experiments; black lines indicate Brillouin zones. (c) The band structure at Cut 1 in (a) and the corresponding second derivative, indicating the existence of TSS marked by the red arrow. (d) The band structure at Cut 2 in (a), showing a flat band near the Fermi level around the K point. (e) EDCs of Cut 2 at different  $K_x$ , showing an ultra-narrow flat band with a large density of states near the Fermi level. (f) Calculated band dispersions along different high-symmetry directions on the Sn-terminated surface of  $Co_3Sn_2S_2$ , showing a nearly flat band (circled) near the Fermi level around the K point, consistent with the experimental observations in (d) [71]. John Wiley & Sons. {@ original copyright notice}.

indicating a giant AHE in the ultra-high-quality  $\text{Co}_3\text{Sn}_2\text{S}_2$  single crystals. Compared to previously reported  $\text{Co}_3\text{Sn}_2\text{S}_2$  samples and other magnetic topological materials, the carrier mobility, MR, anomalous Hall conductivity, and Hall angle of the present crystals rank among the highest.

The intrinsic AHE in magnetic Weyl semimetals originates from Berry curvature associated with bands near Weyl nodes. In  $\text{Co}_3\text{Sn}_2\text{S}_2$ , conduction and valence bands around the nodal ring exhibit opposite Berry curvature contributions, implying a compensating effect between electron and hole carriers. Temperature-dependent transport measurements reveal nearly constant hole density, while electron density decreases with increasing temperature from 2 K to 50 K (figure 5(d)). This depletion has been linked to the presence of an ultra-narrow flat band near the Fermi level (figures 4(d) and (e)), where quantum interference in the kagome lattice suppresses electron kinetic energy and enhances correlations, thereby modulating carrier density.

First-principles calculations further support this picture. Without SOC, multiple nodal rings appear in the BZ, which are gapped upon inclusion of SOC except at two gapless points that evolve into Weyl nodes of opposite chirality (figures 5(e)–(g)). SOC-induced gaps near the nodal rings generate intense

Berry curvature close to the Fermi level (figures 5(h)–(j)). Importantly, the highest valence band (HVB) and lowest conduction band (LCB) exhibit opposite Berry curvature distributions, providing a natural explanation for the bipolar contribution to the AHE. As electron depletion reduces the contribution from the LCB, while the HVB contribution remains unchanged, the net AHC increases with temperature (figures 5(k) and (l)). Calculations further predict that the AHC can be enhanced by nearly 50% at the Fermi level and may reach even higher values upon modest doping or gating, pointing to Co<sub>3</sub>Sn<sub>2</sub>S<sub>2</sub> as a highly tunable platform for Berry-curvature-driven transport phenomena.

In light of the findings above, the iterative-CVT synthesis starting from  $\text{Co}_3\text{Sn}_2\text{S}_2$  single-crystal granules and using NH<sub>4</sub>Cl as the transport agent effectively produces large, high-quality single crystals with superior structural integrity and outstanding physical properties, including flat band, carrier mobility, MR, and the AHE. A particularly striking observation is the  ${\sim}65\%$  enhancement of anomalous Hall conductivity in the low-temperature regime, a behavior arising from the bipolar Berry curvature near the Weyl nodes and the relative balance between electron and hole carriers. Moreover, the presence of an ultra-narrow flat band close to the Fermi level

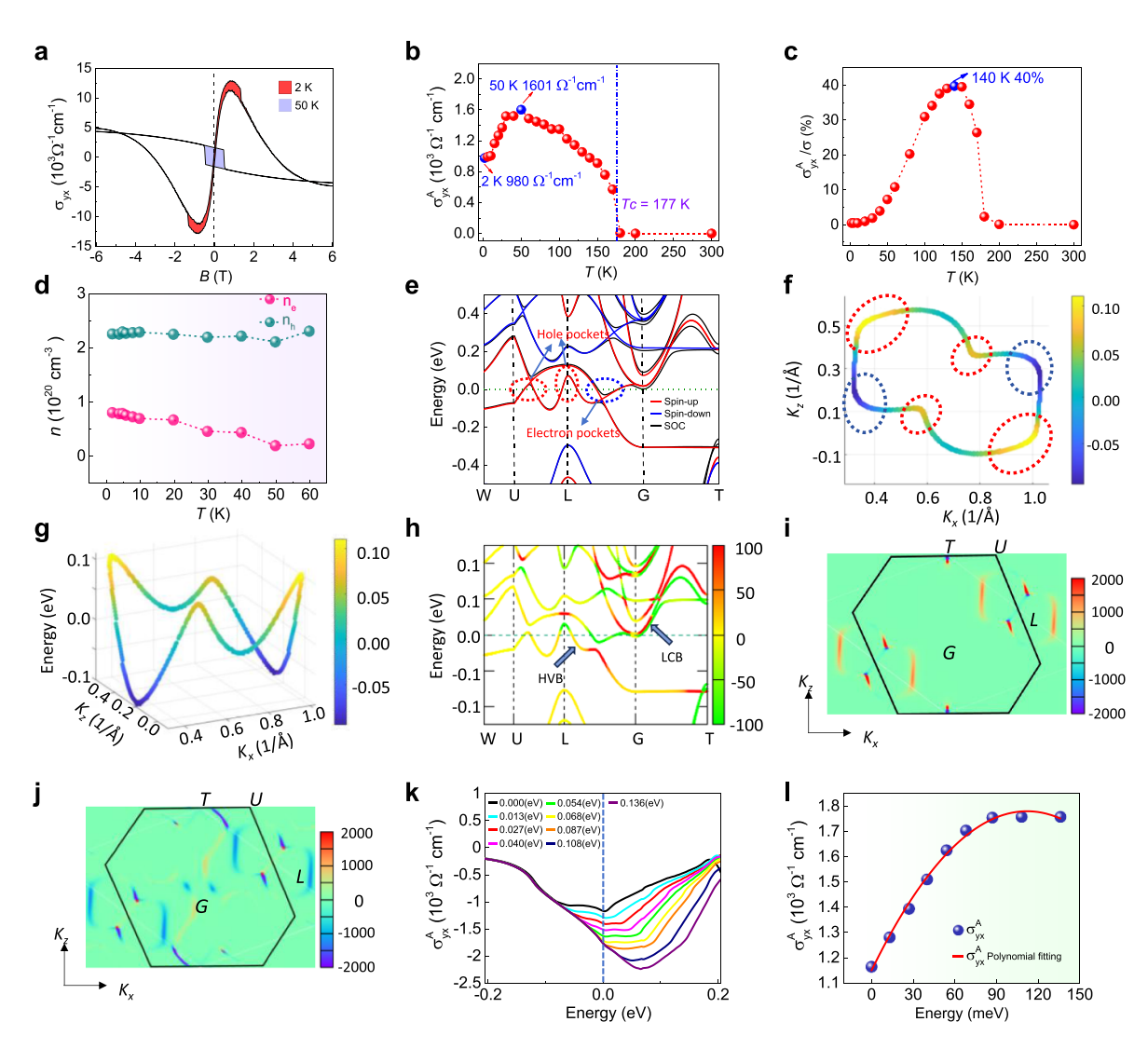


Figure 5. Bipolar AHE in the ultra-high-quality  $Co_3Sn_2S_2$ . (a) Magnetic-field-dependent Hall conductivity  $(\sigma_{yx})$  at 2 K and 50 K under out-of-plane magnetic fields, showing hysteresis behaviors associated to AHE. Shaded areas indicate the AHE contribution. (b) Temperature dependences of the AHC  $(\sigma_{yx}^A)$ , peaking at  $1600 \ \Omega^- \ cm^{-1}$  at 50 K. (c) Temperature dependence of the AHA  $(\sigma_{yx}^A/\sigma)$  at zero magnetic field, showing a maximum of 40% at  $140 \ K$ . (d) Electron and hole concentrations versus temperature. (e) Electronic band structure without and with spin-orbit coupling. (f) Distribution of the nodal ring in the  $k_y = 0$  plane in reciprocal space. Red and blue dashed circles indicate energies above and below the Fermi level, respectively. (g) Energy distribution of the nodal ring. (h) Berry curvature along high-symmetry paths. (i,j) Berry curvature distribution in the  $k_y = 0$  plane corresponding to the LCB and the HVB, respectively. (k) AHC as a function of chemical potential with different electron carrier concentration by shifting of energy of LCB. (l) AHC at the Fermi level as a function of energy shift, extracted from (k) [71]. John Wiley & Sons. {@ original copyright notice}.

amplifies Berry curvature effects and makes the electron density highly sensitive to temperature. The availability of ultrahigh-quality  $\text{Co}_3\text{Sn}_2\text{S}_2$  crystals provides a well-defined platform not only for exploring intrinsic bulk properties but also for examining surface phenomena with precision.

## 3. Surface identification of $\text{Co}_3\text{Sn}_2\text{Sn}_2$ crystals with nc-AFM

Layered quantum materials like Co<sub>3</sub>Sn<sub>2</sub>S<sub>2</sub> often cleave into multiple terminations, each hosting distinct electronic and magnetic states. Accurate identification of these surfaces is therefore crucial, as surface-specific phenomena can strongly

influence the overall behavior of the material and the potential applications in topological and spintronic devices. While STM has provided valuable insights, it cannot always unambiguously distinguish S- and Sn-terminated surfaces due to their nearly identical atomic structures (figure 1(a)). This challenge motivates the use of complementary techniques, such as bondresolved nc-AFM, to resolve surface terminations with atomic precision.

#### 3.1. Four types of cleaved surfaces of Co<sub>3</sub>Sn<sub>2</sub>S<sub>2</sub>

We measured a grid of  $10 \times 10$  points over an area of  $1.1 \times 1.3$  mm<sup>2</sup> of a  $Co_3Sn_2S_2$  sample (figure 6(a)), which

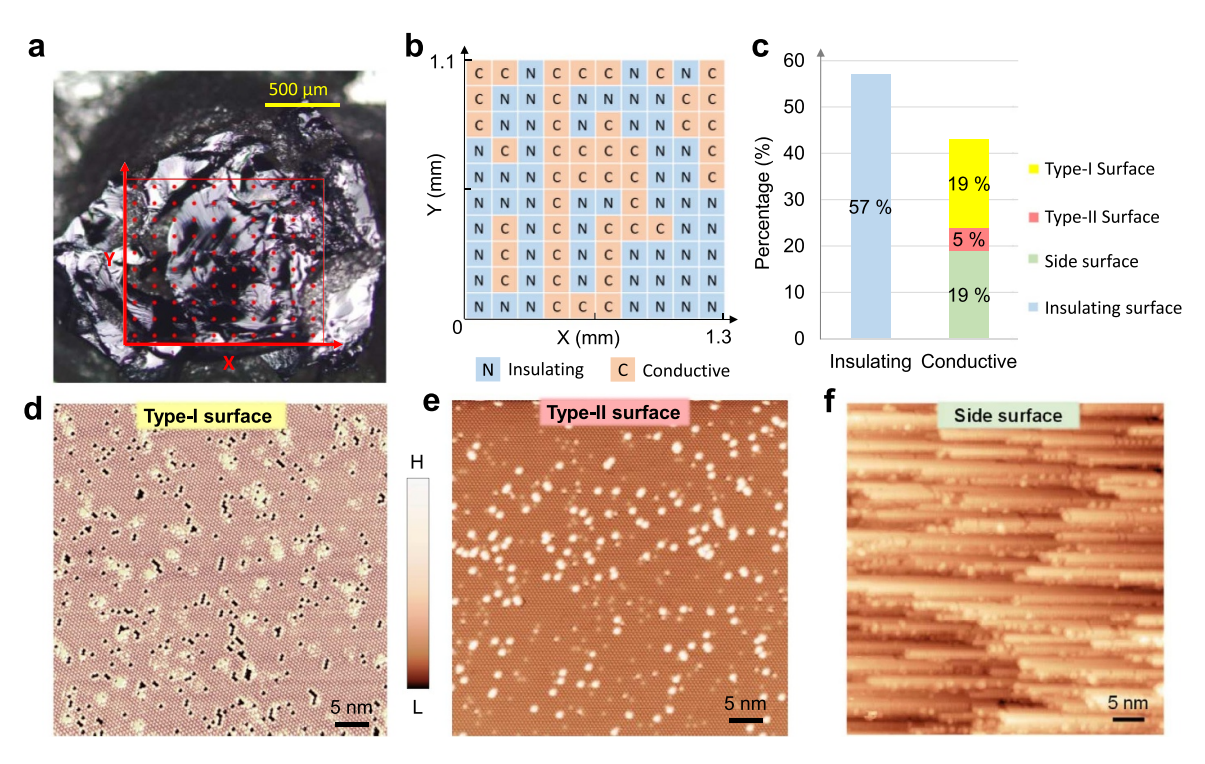


Figure 6. Statistics about surface distributions and STM images of typical surfaces of  $Co_3Sn_2S_2$ . (a) An optical photo of the sample, showing the tested scanning area by the red rectangle. (b) The conductivity distribution of  $10 \times 10$  points over an area of  $1.3 \times 1.1$  mm<sup>2</sup>. The blue squares marked by N denote the insulating surfaces; the orange squares marked by C indicate the conductive surfaces. (c) Statistical analysis of the 100 points in (b). (d)–(f) Large-area STM images of the Type-I, Type-II and side surfaces, respectively.

was cleaved at temperatures below 10 K and transfer to the STM head at 4.5 K within 10 s. Of the 100 points examined, 57 exhibited insulating surfaces (figures 6(b) and (c)), which were previously overlooked in STM studies due to their low conductivity. When approaching these regions with a qPlus sensor, the oscillation amplitude drops to zero upon tipsurface contact, yet the tunneling current fails to reach the setpoint. Typically, the approach halts automatically when the tip penetrates the insulating layer, which can be several nanometers thick. Bulk tin is known to undergo a phase transition from metallic  $\beta$ -phase to semimetallic  $\alpha$ -phase upon cooling, accompanied by a volume expansion of approximately 30% [78–81]. A similar process may also happen with some of the Sn-terminated surface in Co<sub>3</sub>Sn<sub>2</sub>S<sub>2</sub>, leading to the formation of surfaces covered with low-conductivity Sn clusters.

Among the 43 conductive areas examined (figure 6(c)), two distinct types of surface terminations were identified. Nineteen regions exhibit vacancy-decorated surfaces (Type-I, figure 6(d)), whereas five display adatom-decorated surfaces (Type-II, figure 6(e)). The remaining nineteen regions correspond to side surfaces (figure 6(f)), which are likely formed by cleavage along crystallographic planes that are not energetically favored. Typical STM images of both Type-I and Type-II surfaces reveal a triangular lattice structure, in accordance with the symmetry of S- and Sn- terminated surfaces. The absence

of kagome-like features in the STM images, along with theoretical surface energy comparisons, suggests that these are unlikely to be Co<sub>3</sub>Sn-terminated surfaces. Nevertheless, both surfaces exhibit electronic properties that reflect underlying kagome symmetry [59, 72]. The characteristic of Weyl fermions differs between the two surfaces, with Weyl Fermi arc discovering on the Type II surface but absent on the Type I surface [60]. To elucidate the mechanism underlying these surface-dependent properties and clarify how the kagome layers govern the electronic states of the adjacent triangular layers, accurate identification of surface terminations is essential.

However, the surface identification of Type-I and Type-II terminations has been inconsequently presented and continues to be debated [82], as shown in figure 7. STM measurement of a step height between a Co<sub>3</sub>Sn surface and a Type-I surface supported assigning Type-I to the S-terminated surface and Type-II to the Sn-terminated surface [60, 72]. This assignment is further corroborated by surface-dependent properties, such as Fermi arc features, which show good agreement between experiment and DFT calculations [60]. However, STM imaging at the atomic step between the two surface types appears to suggest the opposite [59], leaving the identification unresolved. Since STM cannot give decisive evidence for the surface identification, complementary surface-sensitive techniques such as nc-AFM were strongly needed and employed.

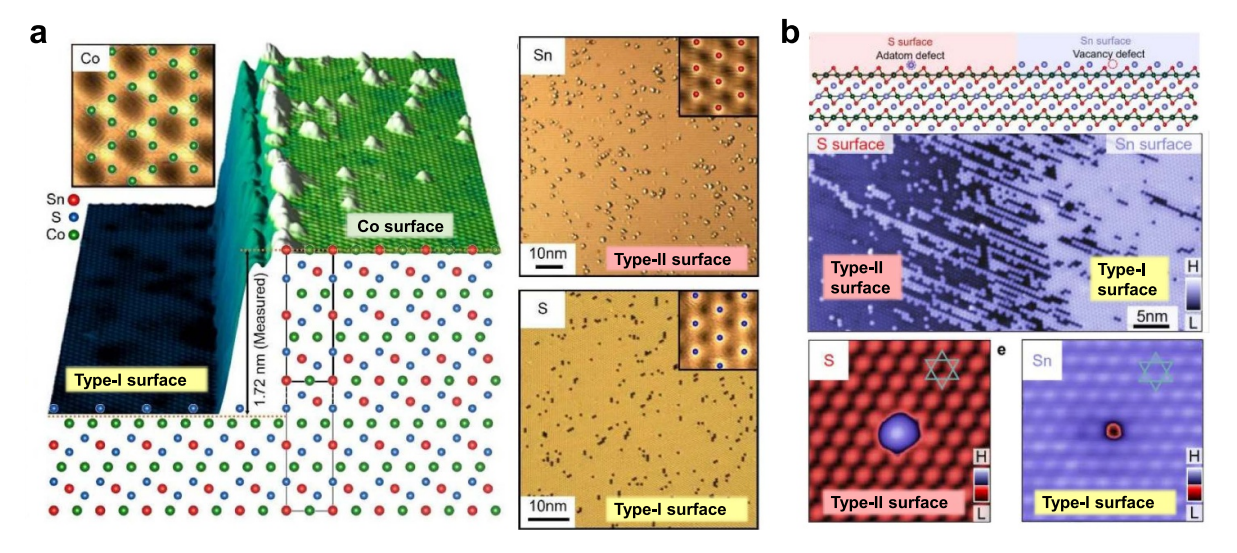


**Figure 7.** Different surface identification of  $Co_3Sn_2S_2$  in previous studies. (a) 3D STM image showing a step between Co- and S-terminated regions with superimposed crystal structure (Co: green, S: blue, Sn: red) and unit cell marked by black line; inset shows atomically resolved Co surface. From [60]. Reprinted with permission from AAAS. (b) Topographic image of the boundary between S-terminated (red) and Sn-terminated (blue) surfaces, with schematic of cleavage-induced defects: Sn adatoms on S surface (left) and Sn vacancies on Sn surface (right). [59, 60, 82]. Reproduced from [59], with permission from Springer Nature.

#### 3.2. Nc-AFM: principle and applications

In nc-AFM measurements, the cantilever is mechanically driven to oscillate at its resonance frequency  $f_0$ . The experiments discussed in this review were performed in frequency modulation (FM) mode, in which a feedback loop maintains a constant oscillation amplitude. During scanning, variations in the tip-surface interactions cause shifts in the cantilever's resonance frequency. A phase-locked loop tracks the actual oscillation frequency  $f = f_0 + \Delta f$ , with the frequency shift  $\Delta f$  serving as the imaging signal.

In FM mode, the cantilever behaves as a harmonic oscillator with a single degree of freedom, and long-range force contributions can be minimized by using a small oscillation amplitude. Assuming that the force gradient is small compared with the cantilever spring constant k and that the oscillation amplitude is much smaller than the tip-sample distance z, the frequency shift  $\Delta f$  can be approximated as:

$$\frac{\Delta f}{f_0} = \frac{f - f_0}{f_0} = \frac{1}{2\pi f_0} \left( \sqrt{\frac{k'}{m'}} - \sqrt{\frac{k}{m'}} \right) \approx -\frac{1}{2k} \frac{\partial F}{\partial z}, \quad (1)$$

where m' is the effective mass of the cantilever, and  $k' = k - (\partial F/\partial z)$  [83]. For small oscillation amplitudes, the frequency shift  $\Delta f$  is approximately proportional to the force gradient. Using the analytical approximation developed by Sader and Jarvis [84, 85], the force spectrum F(z) can be derived from the measured  $\Delta f(z)$  spectrum according to the following expression:

$$F(z) = \frac{2k}{f_0} \int_{z}^{\infty} \left\{ \left[ 1 + \frac{\sqrt{A}}{8\sqrt{\pi (t - z)}} \right] \Delta f(t) - \frac{A^{3/2}}{\sqrt{2(t - z)}} \frac{\partial \left[ \Delta f(t) \right]}{\partial t} \right\} dt.$$
 (2)

The total force acting on the AFM tip near the sample includes contributions from long-range van der Waals and electrostatic forces, which extend over several tens of nanometers, as well as short-range chemical forces, which act over a few angstroms. In UHV experiments, the force spectra described in equation (2) allow the short-range chemical force to be isolated by subtracting the long-range van der Waals and electrostatic background. This procedure provides high-resolution information about the spatial distribution of chemical forces at the surface.

The electrostatic force reflects the work function difference between the tip and the surface and is described as:

$$F_{\text{el.st.}} = \frac{1}{2} \frac{\partial C}{\partial z} (V - V^*)^2, \tag{3}$$

where V is the voltage applied to the sample, and  $V^*$  represents the contact potential difference between the tip and the sample ( $V^* > 0$  means that the work function of the sample is greater than that of the tip). The term  $\partial C/\partial z$  depends on the tip geometry, which is always negative. Based on the Kelvin probe force microscopy (KPFM) measurements [86], the electrostatic force can be minimized by compensating the contact potential difference by choosing  $V = V^*$ . The local contact potential difference (LCPD) is then determined by the position of the maximum of the  $\Delta f(V)$  parabola.

Nc-AFM equipped with a qPlus sensor [87, 88] (figure 8(a)) is renowned for imaging short-range interactions at the single-chemical-bond level [89–100], and has been pushing the limit of detecting physical or/and chemical interactions [101–106]. Unlike STM images that provide information on delocalized states, nc-AFM images sensitively reflect the spatial gradient of short-range repulsive interactions, e.g. Pauli repulsion, resulted from localized electronic states. Thus, it shows unprecedented resolution on locating electronic orbitals and/or

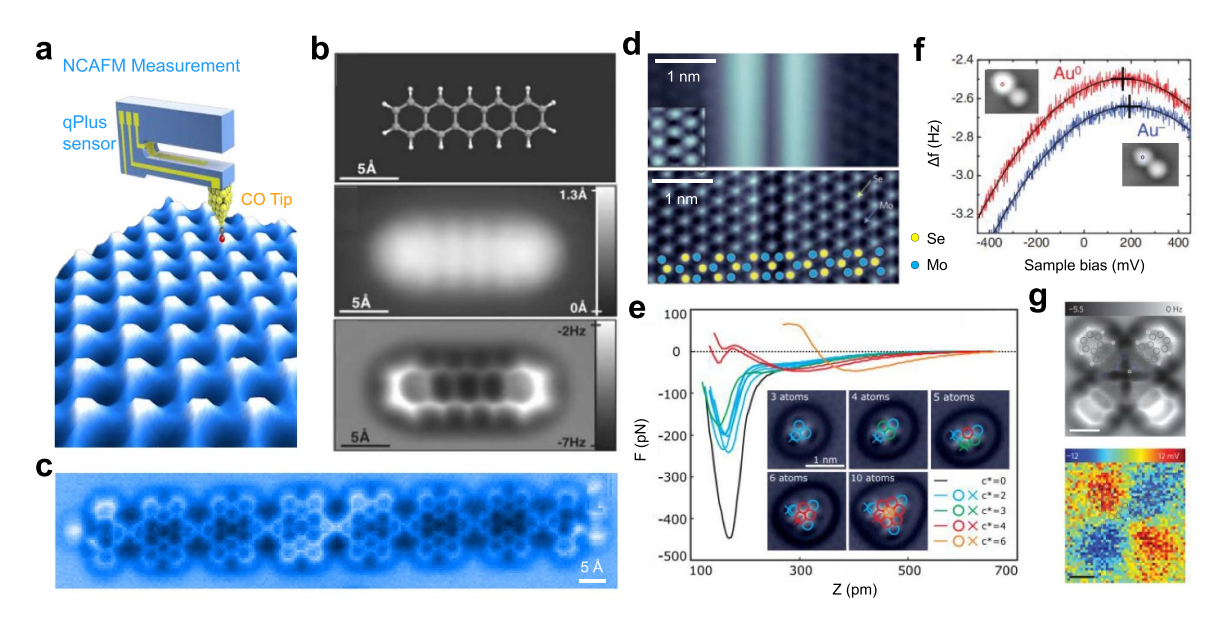


Figure 8. Schematic of the nc-AFM setup and representative applications for atomic-scale imaging and surface characterization. (a) Schematic of the nc-AFM measurements, which are based on a qPlus sensor with a CO-functionalized tip in frequency modulation mode. Reproduced from [70]. CC BY 4.0. (b) STM and nc-AFM imaging of pentacene on Cu(111). While the STM images the frontier orbitals, the nc-AFM image clearly resolved the chemical bonds. From [89]. Reprinted with permission from AAAS. (c) Chemical-bond-resolved nc-AFM image of a diaza-HBC chain. Reproduced from [99], with permission from Springer Nature. (d) STM and nc-AFM images of a mirror twin boundary in monolayer MoSe<sub>2</sub>. The surface Se atoms are resolved in the nc-AFM images. Reproduced from [108], with permission from Springer Nature. (e) F(z) curves measured on top of Fe atoms in clusters of different sizes, reflecting their different chemical reactivity. Reprinted (figure) with permission from [105], Copyright (2009) by the American Physical Society. (f)  $\Delta f(V)$  curves measured on neutral and negatively charged Au adatoms by nc-AFM KPFM mode, showing their different charge states. From [111]. Reprinted with permission from AAAS.(g) Charge distribution within a single naphthalocyanine molecule resolved by nc-AFM KPFM mode. Reproduced from [112], with permission from Springer Nature.

interactions [89, 107] and uncovering crystalline domain walls and defects (figures 8(b)–(d)) [108]. Furthermore, by measuring height-dependent frequency shifts on different locations of a surface [109], nc-AFM is empowered of identifying localized chemical environment on the surface (figure 8(e)) [103, 105, 107, 110]. In addition, this technique can probe the chemical potential in atomic resolution by measuring the LCPD acquired with KPFM mode (figures 8(f) and (g)) [111–113].

## 3.3. Identification of S surface by work function measurements and bond-resolved nc-AFM imaging

The STM topographies reveal vacancies on the Type-I surface (figures 9(a) and (b)) and adatoms on the Type-II surface (figures 9(d) and (e)). To distinguish the two surfaces, LCPD was measured on both surfaces by recording the frequency shift ( $\Delta f$ ) as a function of sample bias (V) (figure 9(g)). The  $\Delta f$ (V) measurements show maxima at -0.22 V for Type-I and +0.57 V for Type-II, indicating that Type-I has a work function  $\sim 0.79$  eV higher than Type-II (figure 9(h)). As a reference, the work function is calculated to be 5.29 eV, 4.34 eV and 4.61 eV for the S-, Sn- and Co<sub>3</sub>Sn-terminated surfaces, respectively, indicating that the S surface has the highest work function (0.95 eV higher than the Sn surface and 0.68 eV higher than the Co<sub>3</sub>Sn surface). This correspondence supports assigning Type-I to the S-terminated surface, while Type-II is

more consistent with Sn- or Co<sub>3</sub>Sn-termination, although distinguishing between the two remains challenging due to their similar work function values.

To further concrete the surface assignment, a CO-functionalized tip [89, 114, 115] was employed for imaging both surfaces in chemical-bond resolution. In the nc-AFM image of the S surface (figures 9(c) and 10(a)), the surface S atoms appear as bright spots with slight anisotropy (region  $\alpha_I$ ), forming a well-defined triangular pattern. A higher-resolution image reveals three line-like features radiating from each S atom, symmetrically arranged with respect to rotational angle. These lines converge into diffuse areas (region  $\beta_I$ ), while the surrounding darker areas are designated as region  $\gamma_I$ .

The Type-II surface exhibits distinct triangular features in regions  $\alpha_{\rm II}$  and  $\beta_{\rm II}$ , which connect to form a 2D breathing kagome pattern (figures 9(f) and 10(d)). The kagomelike appearance of the Type-II surface resembles that of the Co<sub>3</sub>Sn layer, although this termination is less stable than the Sn layer when exposed at the surface [60]. As neither the Sn nor the Co<sub>3</sub>Sn -terminated surface fully accounts for both the observed contrast and the lower surface energy, the assignment of the Type-II surface needs further experimental support. Force spectroscopy measurements combined with DFT calculations provide decisive evidence that the Type-II surface corresponds to the Sn termination, which can indeed host a kagome-like electronic pattern [70].

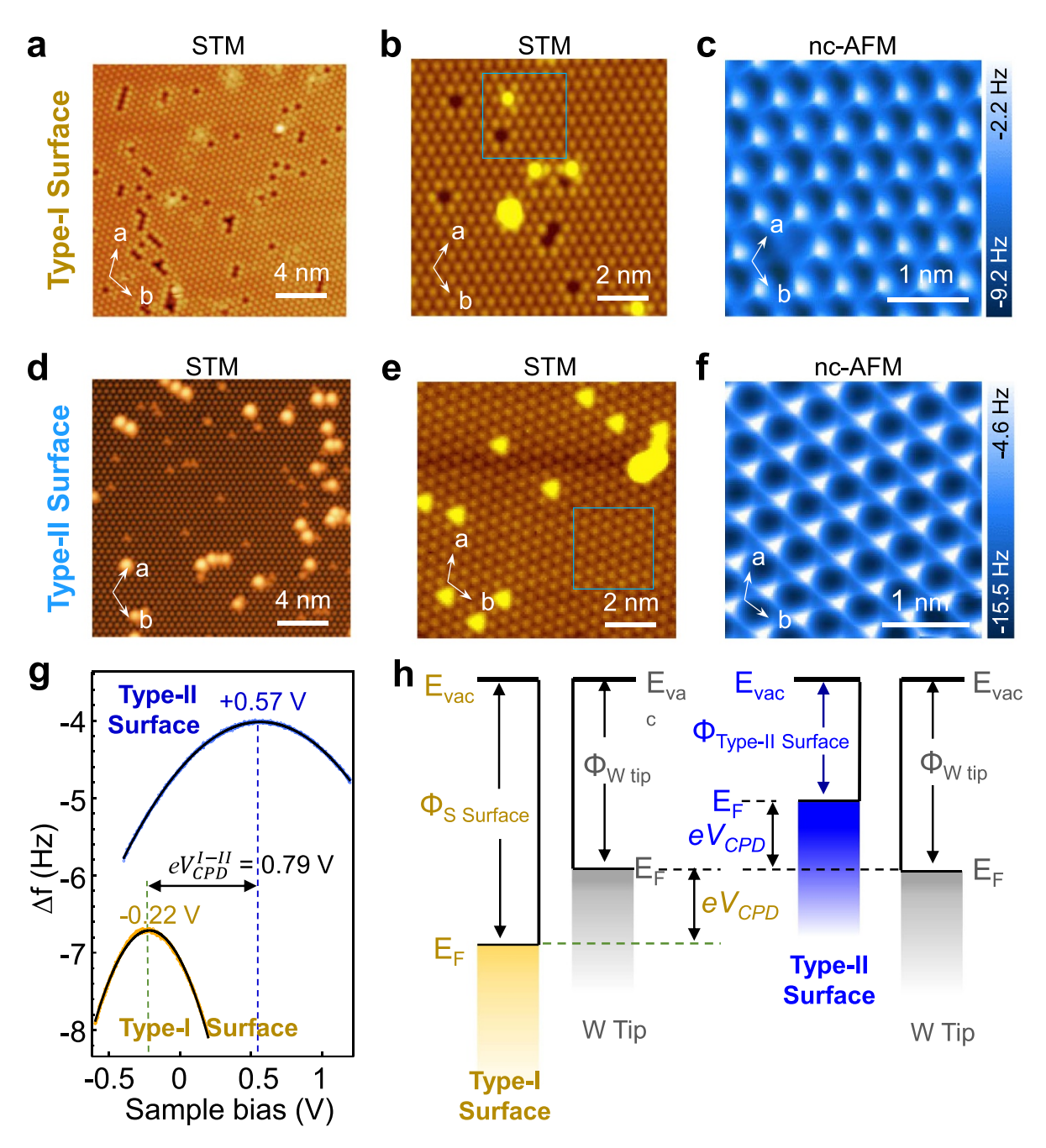


Figure 9. Nc-AFM images and work function measurements of the Type-I and Type-II surfaces in  $Co_3Sn_2S_2$ . (a), (b) large-area and zoom-in STM images of the Type-I surface of  $Co_3Sn_2S_2$ . (c) Chemical-bond-resolved nc-AFM image of the Type-II surface taken in the blue square in (b). (d), (e) Large-area and zoom-in STM images of the Type-II surface of  $Co_3Sn_2S_2$ . (f) Chemical-bond-resolved nc-AFM image of the Type-II surface taken in the area marked by a blue square in (e). (g)  $\Delta f(V)$  curves on Type-I and Type-II surfaces. The maxima of the  $\Delta f(V)$  parabolas are located at -0.22 V and +0.57 V for Type-I and Type-II surfaces, respectively. The work function difference between the two surfaces is 0.79 eV. (h) Schematic of the relationship between work function and LCPD ( $V_{CPD}$ ) of the Type-I and the Type-II surfaces, respectively.  $V_{CPD} = \frac{\Phi_{tip} - \Phi_{sample}}{-e}$ .  $eV_{CPD}$  is the difference of the work function between the sample surface and tip.  $\Phi_{tip}$  is the work function of the tip,  $\Phi_{Type-II}$  surface the work function of the Type-II surface. Based on the nc-AFM measurements shown in (g),  $\Delta\Phi_{I} = \Phi_{tip} - \Phi_{type-II}$  surface  $= -eV_{CPD}^{I} = 0.22$  eV;  $\Delta\Phi_{II} = \Phi_{tip} - \Phi_{type-II}$  surface  $= -eV_{CPD}^{I} = 0.22$  eV;  $\Delta\Phi_{II} = \Phi_{tip} - \Phi_{type-II}$  surface  $= -eV_{CPD}^{I} = 0.22$  eV; thus,  $\Delta\Phi_{I-II} = \Delta\Phi_{I} \Delta\Phi_{II} = 0.79$  eV. [70, 72]. Reproduced from [70]. CC BY 4.0.

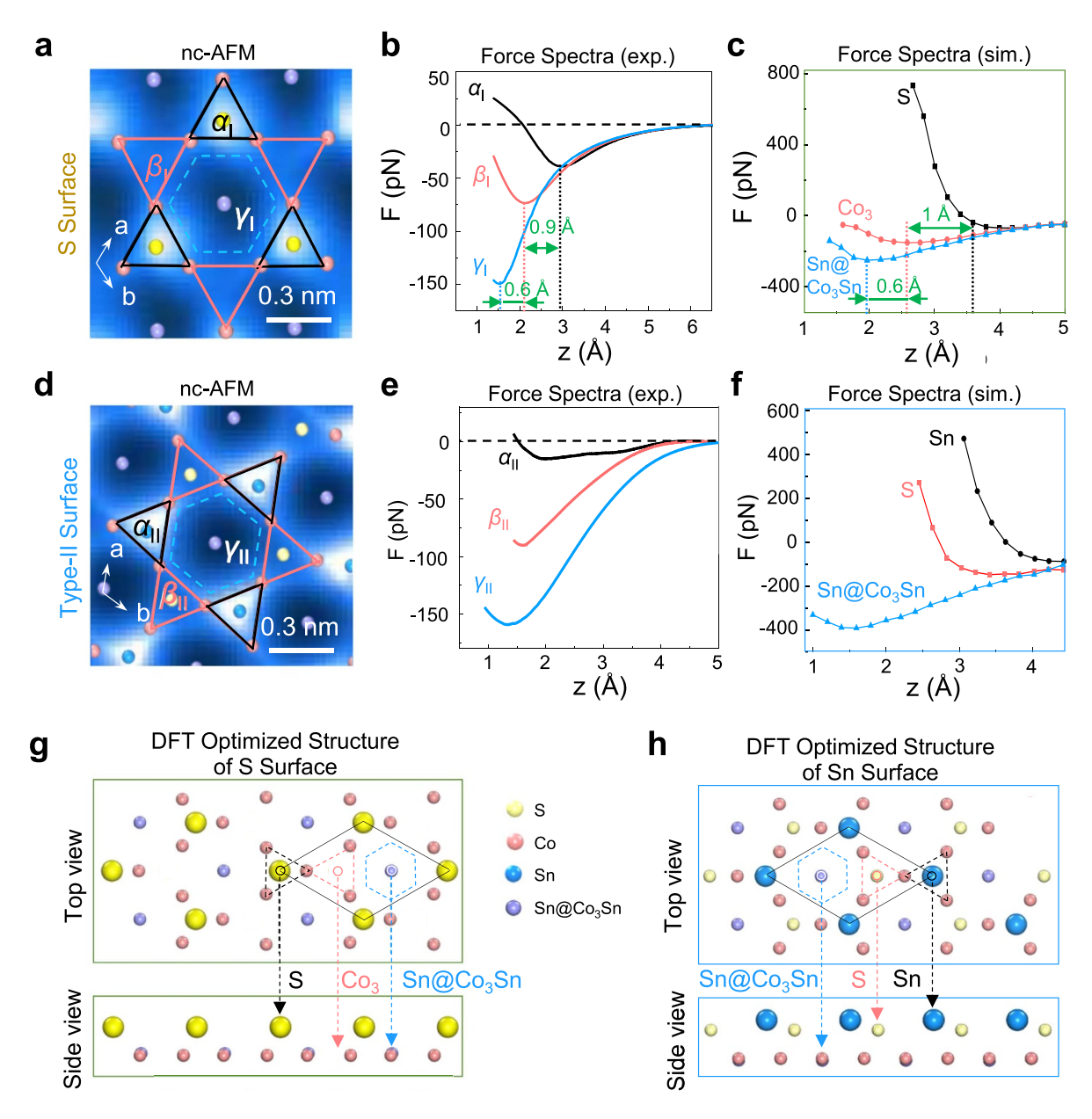


Figure 10. Short-range force spectra on S surface and Type-II surface. (a) Zoomed-in nc-AFM image to show the incomplete kagome pattern on S surface. Three distinct regions within a unit cell with bright, blurry, and dark contrast, which are marked by black solid line triangles, red solid line triangles, and a blue dashed line hexagon, are labeled as  $\alpha_I$ ,  $\beta_I$ , and  $\gamma_I$  regions. The atomic structure of S surface with the underlying Co<sub>3</sub>Sn plane is superimposed. (b) Vertical short-range force spectra measured at the center of the  $\alpha_I$  (black),  $\beta_I$  (red), and  $\gamma_I$  (blue) regions. (c) DFT-calculated force spectra for the S-terminated surface. (d) Zoomed-in nc-AFM image showing the kagome pattern on Type-II surface. Three distinct regions within a unit cell with bright, blurry, and dark contrast, which are marked by black solid line triangles, red solid line triangles, and a blue dashed line hexagon, are labeled as  $\alpha_{II}$ ,  $\beta_{II}$ , and  $\gamma_{II}$  regions. The atomic structure superimposed is the Sn surface with the underlying S and Co<sub>3</sub>Sn plane. (e) Vertical short-range force spectra measured at the center of the  $\alpha_{II}$  (black),  $\beta_{II}$  (red), and  $\gamma_{II}$  (blue) regions. (f) DFT-calculated force spectra for the Sn-terminated surface, showing good agreement with experiment. (g) DFT optimized surface structure on the S surface. (h) DFT optimized surface structure on Sn surface. Reproduced from [70]. CC BY 4.0.

## 3.4. Determination of Sn surface by short-range force spectroscopy

Short-range force spectroscopy has been applied to the relatively well-understood S-terminated (Type-I) surface to establish consistency between experiment and theory. As shown in figure 10(b), the force spectra at regions  $\alpha_{\rm I}$ ,  $\beta_{\rm I}$ , and  $\gamma_{\rm I}$  all exhibit a turning point below 3 Å, with the  $\alpha_{\rm I}$ 

region is 0.9 Å higher than  $\beta_I$  region and  $\gamma_I$  region 0.6 Å lower. Based on the symmetry (figure 10(g)), these regions are tentatively assigned to the top-layer S atom (black dashed triangle), the Co<sub>3</sub> trimer (red dashed triangle), and the Sn atom (blue dashed hexagon) in the underlying Co<sub>3</sub>Sn layer, respectively. The DFT calculated turning-point heights exhibit excellent agreement with experiment (figure 10(c)) -0.9 Å versus 1.0 Å for the  $\alpha_I$  region, and 0.6 Å versus 0.6 Å for the

 $\gamma_{\rm I}$  region—strongly supporting the tentative structural assignments. This close correspondence between experimental and theoretical results further consolidates the identification of the Type-I surface as S-terminated and highlights force-spectra comparison as a reliable approach for determining surface terminations in  $\text{Co}_3\text{Sn}_2\text{S}_2$ .

Figure 10(e) presents the experimental force spectra acquired on the Type-II surface. Among the three regions, the  $\alpha_{\rm II}$  region (black) exhibits the weakest attraction and reaches the turning point first at 1.92 Å. By contrast, the  $\beta_{\rm II}$ , and  $\gamma_{\rm II}$  regions have their turning points at 1.60 Å and 1.31 Å, respectively, with the  $\gamma_{\rm II}$  region characterized by the strongest attractive interaction.

The force spectra on both the Co<sub>3</sub>Sn- and Sn-terminated surfaces were simulated using DFT calculations. The analysis focuses on the relative positions of the turning points for the three characteristic regions, which remain qualitatively unaffected by different tips [105]. On the Co<sub>3</sub>Sn surface, structural relaxation leads to an upward displacement of the topmost Sn atoms by approximately 0.42 Å. The simulated force curves indicate that the Sn site exhibits the earliest turning point and the strongest repulsive interaction, whereas the Co<sub>3</sub>/Sn and Co<sub>3</sub>/S are comparatively less repulsive. This behavior deviates from the experimental observations, where the triangular regions are associated with stronger repulsion. Such discrepancies rule out the Co<sub>3</sub>Sn termination as the Type-II surface.

The Sn-terminated surface is characterized by a triangular lattice of top-layer Sn atoms, accompanied by S atoms arranged in the same lattice but shifted by (1/3, 1/3) and positioned 0.56 Å lower. Each Sn or S atom resides above a Co<sub>3</sub> trimer, giving rise to triangular regions, while the Sn atom embedded within the Co<sub>3</sub>Sn layer (Sn@ Co<sub>3</sub>Sn) defines a hexagonal region. Within this framework, the triangular lattices of Sn and S are assigned to regions  $\alpha_{\rm II}$  (black) and  $\beta_{\rm II}$  (red), respectively, whereas the Sn@ Co<sub>3</sub>Sn hexagon corresponds to region  $\gamma_{\rm II}$  (blue). Theoretical force spectra (figure 10(f)) reproduce the experimental trends, capturing both the order of repulsion strengths and the relative turning points. This agreement provides compelling evidence that the Type-II surface corresponds to the Sn termination of Co<sub>3</sub>Sn<sub>2</sub>S<sub>2</sub>.

By combining work function measurements, bond-resolved nc-AFM imaging, vertical short-range force spectroscopy, and DFT calculations, the surface terminations of  $\text{Co}_3\text{Sn}_2\text{S}_2$  have been unambiguously determined. Type-I is identified as the Sterminated surface, and Type-II as the Sn-terminated surface. Furthermore, they highlight the capability of nc-AFM as a powerful tool for characterizing surface terminations and localized electronic states at single-bond resolution. The decisive determination of the cleaved surfaces provides a solid foundation for further investigations and understanding of the interplay between lattice geometry, SOC, and electron correlations in  $\text{Co}_3\text{Sn}_2\text{S}_2$ .

#### 4. SOPs on S surface: discovery and manipulation

Atomic-scale defects often play a crucial role in shaping the physical properties of topological quantum materials, and their

influence becomes particularly prominent in systems with strong SOC and magnetic order. In Co<sub>3</sub>Sn<sub>2</sub>S<sub>2</sub>, vacancies on the S surface have been shown to give rise to an emergent localized excitation termed as the SOP, which exhibits a rich interplay between magnetism and topology.

#### 4.1. Localized SOPs induced by the S vacancies

On the S-terminated surface, there are many randomlydistributed S vacancies (figure 11(a)). The dI/dV spectrum near S vacancies reveals a series of discrete, approximately equally spaced in-gap states just above the valence band edge (figure 11(b)), indicating the formation of vacancyinduced bound states. Conductance maps recorded at the most prominent resonances (at -322, -300, and -283 mV) display distinct, localized features with a characteristic flowerpetal shape (figure 11(c) shows the map at -283 mV). Each of these patterns exhibits clear three-fold rotational symmetry centered at the vacancy, with spatial extent reaching out to the six nearest-neighbor S atoms (figure 11(d)). The brightest intensity is concentrated on three up-triangles of the underlying kagome lattice nearest to the vacancy (highlighted by red dashed lines in figure 11(c)), illustrating that the bound state polaron is driven by the localization of Co d-electrons underlying the vacancy, in hybridization with S *p*-electrons.

These bound states were found to be intrinsically spin-polarized. Spin-polarized STM measurements, using bulk nickel (Ni) tips, demonstrated strong spin asymmetry at the vacancy site, with a clear dominance of spin-down states in the energy range of the polaronic resonances (figure 11(f)). In contrast, it shows spin symmetric features off vacancy site (figure 11(f)). Notably, with a spin flip operation of the Ni tip, the intensity of the bound states varies accordingly, indicating its spin-polarized nature (figure 11(g)).

More intriguingly, the application of out-of-plane magnetic fields caused a uniform shift of the bound states to higher energy, regardless of the field direction (figures 12(a) and (b)). This unusual behavior corresponds to anomalous Zeeman response, revealing that the magnetic moment at the S vacancy is dominated by a diamagnetic orbital component [59]. To highlight its orbital magnetic moment, the magnetic bound state is dubbed as a localized SOP [72]. Fitting the two sub-peak positions as a linear function of the magnetic field (figure 12(c)), an effective orbital magnetic moment of approximately 1.35  $\mu_B$  was extracted. Such a large orbital moment is a hallmark of topologically nontrivial orbital magnetism [59]. Theoretical calculations suggest that this orbital response originates from diamagnetic circulating currents induced by the local electronic structure around the defect. The strong Berry curvature inherent to the Weyl semimetallic state of Co<sub>3</sub>Sn<sub>2</sub>S<sub>2</sub> provides a natural environment for such topological orbital effects to arise. The formation of SOPs, therefore, reflects a unique synergy between the localized real-space physics of atomic defects and the global momentum-space topology of the host material.

The magnetoelastic coupling associated with localized SOPs has been revealed by STM (figure 12(d)) and nc-AFM

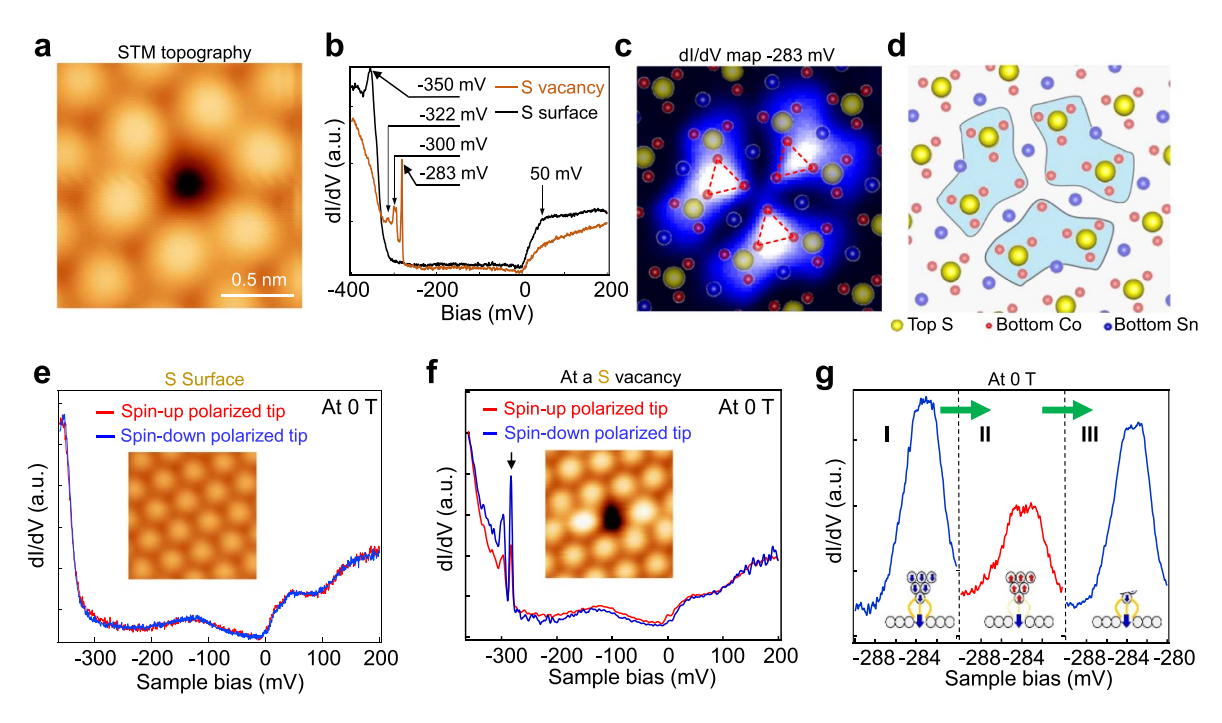


Figure 11. Spin-polarized bound states at a single S vacancy at the S-terminated surface of  $Co_3Sn_2S_2$ . (a) STM image of an S vacancy. (b) dI/dV spectra on (orange) and off (black) the vacancy. (c), (d) dI/dV map at -283 meV and correlation with the atomic structure, showing bound-state distribution aligned with Co atoms. (e) Spin-polarized dI/dV spectra on pristine S surface with up-polarized (red) and down-polarized (blue) tips, showing negligible contrast. (f) dI/dV spectrum at a single S vacancy revealing spin-down majority; inset: STM image (2 nm  $\times$  2 nm). (g) Spin-flip operation of the STM tip, with spectra corresponding to spin-down (I), spin-up (II), and flipped back to spin-down (III) polarizations. Reproduced from [72]. CC BY 4.0.

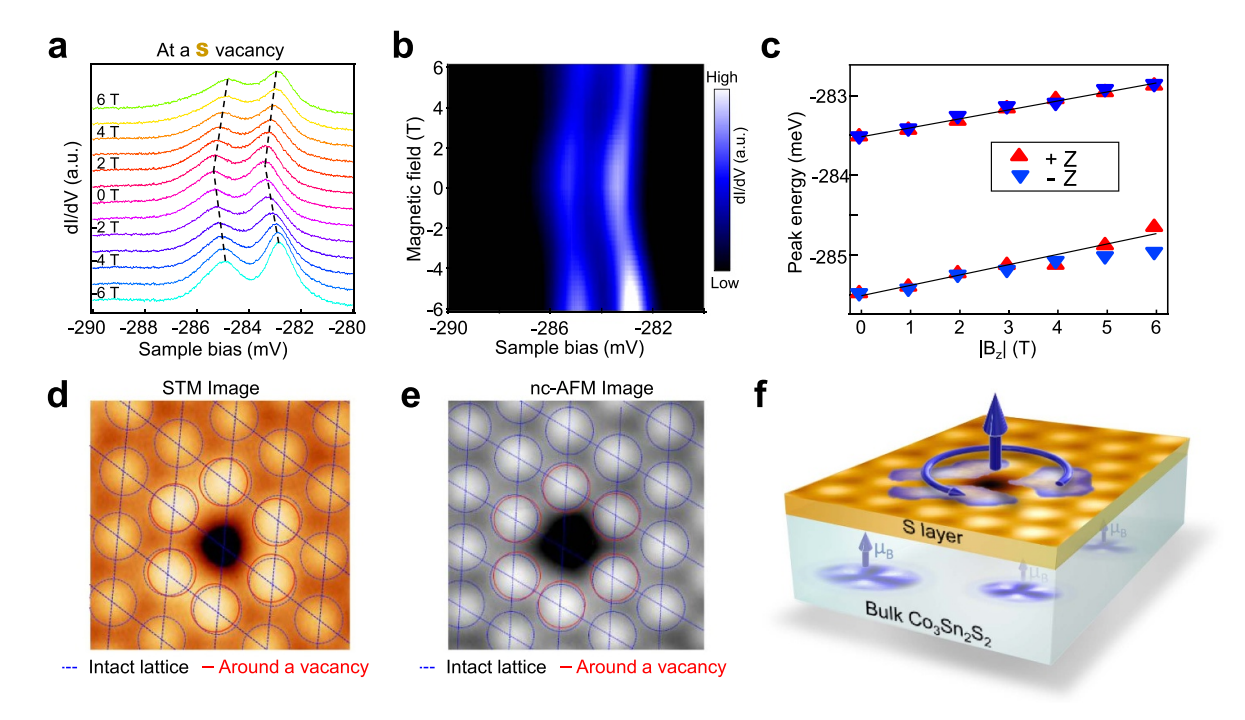


Figure 12. Anomalous Zeeman shift of the bound states and spin–orbit polaron at a single S vacancy. (a) dI/dV spectra under perpendicular magnetic fields from -6 T to 6 T show a linear energy shift towards high energy independent of field direction, with the corresponding intensity map in (b) and peak energy shifts plotted against field magnitude in (c). (d), (e) STM and nc-AFM images (2.3 nm  $\times$  2.3 nm) of a single S vacancy reveal local lattice distortion. (f) Schematic illustration of a localized spin–orbit polaron in  $Co_3Sn_2S_2$ . Reproduced from [72]. CC BY 4.0.

images (figure 12(e)), which show lattice distortions around sulfur vacancies with appreciable local atomic displacements even at zero magnetic field. The average nearest-neighbor distances around the vacancies, expressed as a displacement ratio relative to intact regions, decrease significantly with increasing magnetic field applied along the c-axis. Remarkably, up to one-third of the displacement ratio can be tuned by a field of 6 T, providing compelling evidence for the polaronic nature of these bound states and their strong magnetoelastic coupling in  $\text{Co}_3\text{Sn}_2\text{S}_2$ .

The localized SOPs observed in Co<sub>3</sub>Sn<sub>2</sub>S<sub>2</sub> arise from the interplay of correlated magnetism, strong SOC, and topological characteristics of the Weyl semimetal phase. Both itinerant and localized magnetism originate from Co 3d electrons, which hybridize with Sn and S p orbitals on a kagome lattice with frustrated kinetic energy. S vacancies, located off the kagome plane, serve as local perturbations that trap Co d-electrons, forming discrete bound states with pronounced orbital magnetization, as revealed by their spin sensitivity and anomalous Zeeman behavior. This orbital magnetism stems not only from the Berry curvature of the localized d-states, but also from the magnetoelectric coupling inherent to Weyl fermions, reminiscent of topological insulator systems where magnetic perturbations induce persistent orbital currents and large orbital magnetization [116, 117]. Moreover, the fact that such states emerge from a single sulfur vacancy underscores the potential of defect engineering as a means to tune the topological and magnetic properties of kagome systems, as further discussed below.

## 4.2. Atomically precise engineering of the spin-orbit polarons

Leveraging the high spatial precision of low-temperature STM, SOPs can be manipulated by voltage pulses from the STM tip (figure 13(a)). These manipulations enable both the removal and reconstruction of S vacancies, offering a deterministic route to engineer the geometry and coupling of SOPs [73].

The vacancy repair process is initiated by applying a positive voltage pulse (e.g. +3.2 V for 10 ms), which lifts a S atom from the subsurface layer to fill in the surface vacancy and restore the local lattice (figures 13(b)–(d)). This process is reversible: a negative voltage pulse (e.g. -3.2 V for 10 ms) can re-create a vacancy by removing a top-layer sulfur atom (figures 13(e)–(g)). The vacancy formation and healing were verified via repeated cycles on the same surface site (figures 13(h) and (i)). Statistical data show a vacancy healing success rate of  $\sim 30\%$ , compared to a lower  $\sim 5\%$  for vacancy creation, likely due to the more favorable energy barrier of upward S diffusion compared to removing S atoms from the lattice.

This tip-induced vacancy manipulation allows for the controlled fabrication of arbitrary SOP configurations, such as linear chains, triangular clusters, and hexagonal arrays. These structures act as building blocks for artificial quantum states with tunable spatial and spectral characteristics. STM images

show that vacancies can be placed with single-atom precision, and the resulting configurations remain stable at low temperatures, providing a reliable platform for studying interactions between neighboring SOPs (figures 14(a)–(h)).

Spectroscopic measurements reveal that each SOP configuration supports a set of discrete in-gap states with equally spacing energy, and the most intense peak (P(N)) shifting systematically with vacancy size N (defined as the number of S vacancies). As shown in figure 14(i), the evolution of P(N) for vacancies of different symmetric shapes follows an exponential function, with P(N) approaching a shape-dependent critical energy near the Fermi level as the vacancy size increases. The critical energy varies with geometry, where higher-symmetry shapes exhibit higher critical energy levels. For example, P(N) for single-chain vacancies saturates around -240 meV, whereas that for hexagonal vacancies approaches the Fermi level

This shift of peak energy with the size and shape of vacancy reflects enhanced wavefunction delocalization and hybridization between neighboring SOPs, analogous to band formation in coupled quantum dot systems. For instance, in 1D chain configurations, the bound states exhibit dispersive, bandlike features, whereas in compact geometries (e.g. triangular clusters), quantum confinement dominates. To understand the shape-dependent energy shifts of P(N), a simple tight-binding model with nearest-neighbor hopping t was used to simulate bound states around vacancies. Four vacancy patterns single chain, double-column chain, triangle, and hexagonwere analyzed. For each configuration, the highest energy level was taken as the vacancy state. The calculations show that this vacancy state shifts exponentially toward higher energy with increasing size (figure 14(k)), consistent with the experimental trends.

The magnetic character of SOPs is preserved across these engineered configurations. Spin-polarized STM measurements reveal that SOPs consistently show a spin-down dominant signal at the bound-state energies, regardless of vacancy geometry. This spin asymmetry confirms that the SOPs carry localized magnetic moments, which can be probed and modulated by external magnetic fields. Under out-of-plane magnetic fields (up to  $\pm 6$  T), the primary bound state P(N) exhibits an anomalous Zeeman shift, which deviates from that expected for conventional spin moments and indicates a dominant orbital magnetic contribution.

Fitting the Zeeman shift shows that the effective magnetic moment increases with vacancy size, from about 1.5  $\mu_B$  for small triangular SOPs to nearly 3  $\mu_B$  for larger triangular and hexagonal vacancies. The correlation between vacancy geometry, bound state energy, and magnetic moment underscores the complex interplay between real-space structure and topological electronic states. As such, SOPs provide a unique opportunity to engineer artificial magnetic and orbital textures on kagome surfaces. With increasing vacancy size or coupled SOP arrays, it becomes possible to tune not only the magnetic moment, but also the spatial symmetry and coherence length of the emergent states.

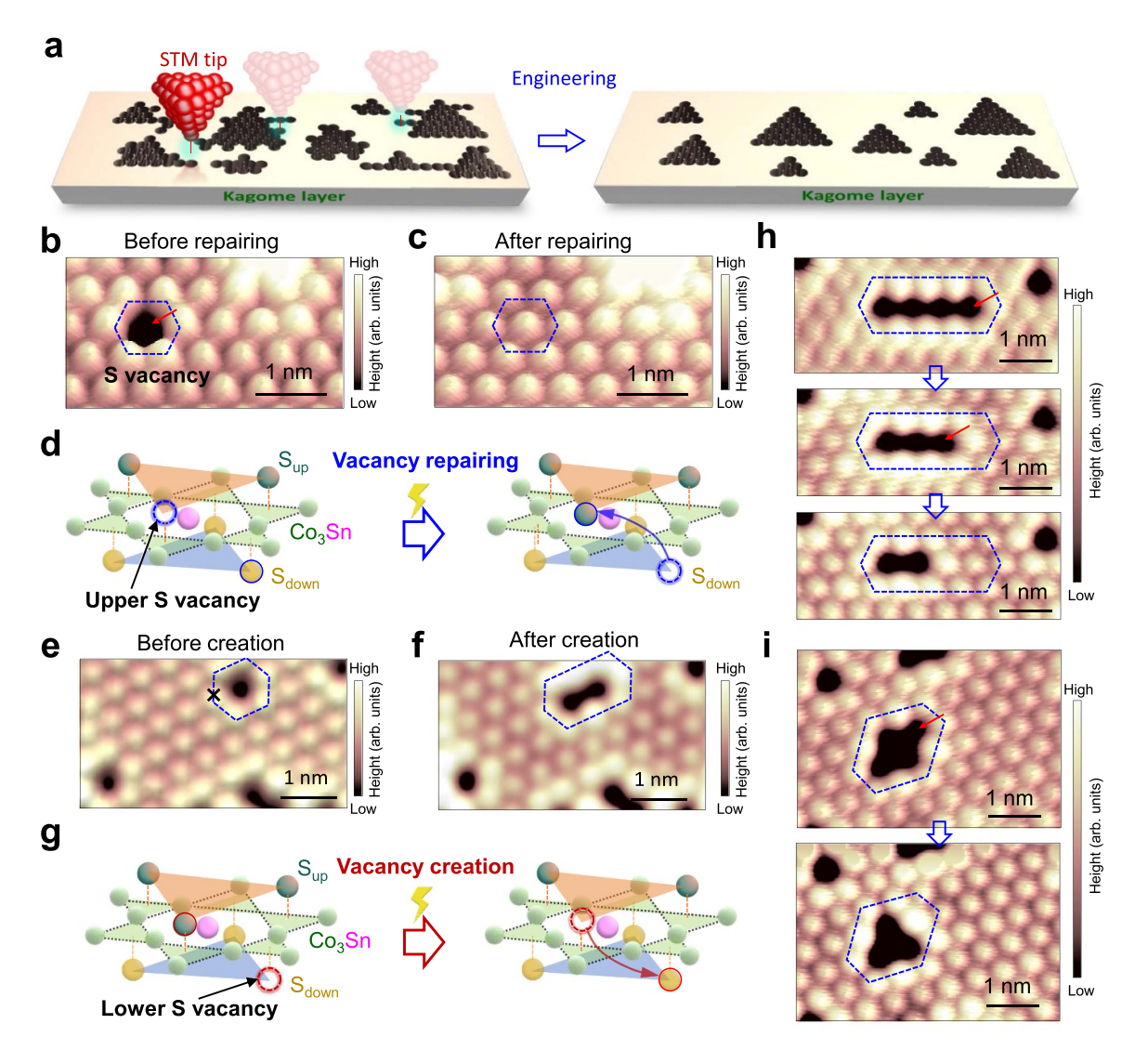


Figure 13. Atomically precise engineering of vacancies at S-terminated surface of  $Co_3Sn_2S_2$ . (a) Schematic of tip-assisted vacancy engineering, transforming irregular vacancies into well-defined geometries. (b), (c) STM images before and after vacancy repair, with the red arrow marking the tip pulse. (d) Schematic of S atom filling from the bottom S layer. (e), (f) STM images before and after vacancy creation, with the black cross indicating the tip pulse. (g) Schematic of S removal from the top layer filling a bottom-layer vacancy. (h) STM sequence showing gradual shortening of a vacancy chain. (i) STM sequence showing transformation of a cross-shaped vacancy into a triangular one, with red arrows marking tip pulses. Reproduced from [73]. CC BY 4.0.

The discovery of SOPs in Co<sub>3</sub>Sn<sub>2</sub>S<sub>2</sub> provides a new way to manipulate magnetic order and topological phenomena. STM studies show that S vacancies on low-temperature cleaved S-terminated surfaces reflect bulk S vacancies, where SOPs are expected to form. DFT calculations reveal that these vacancies are magnetic and enhance the moments of neighboring Co atoms. The density of SOPs can therefore be tuned by controlling S pressure and temperature during synthesis. Increased SOP density strengthens ferromagnetic moments, enhances carrier scattering by spin—orbit exchange fields, and promotes exchange interactions between SOPs, enabling robust time-reversal-symmetry-breaking effects such as the anomalous Hall and Nernst responses at higher temperatures. Similar to single-defect engineering in diamond [118], controlled

creation of SOPs may open routes to generating large magnetic moments in topological semimetals and toward applications in functional quantum devices.

## 5. Oxygen-induced quantum clusters on Sn and S surfaces

The discovery and manipulation of SOP demonstrate how atomic-scale defects in  $\text{Co}_3\text{Sn}_2\text{S}_2$  can host highly tunable localized quantum states that strongly couple to the material's topological electronic structure. Beyond sulfur vacancies, heteroatom dopants can also shape the local electronic and magnetic properties. In particular, oxygen dopants, which

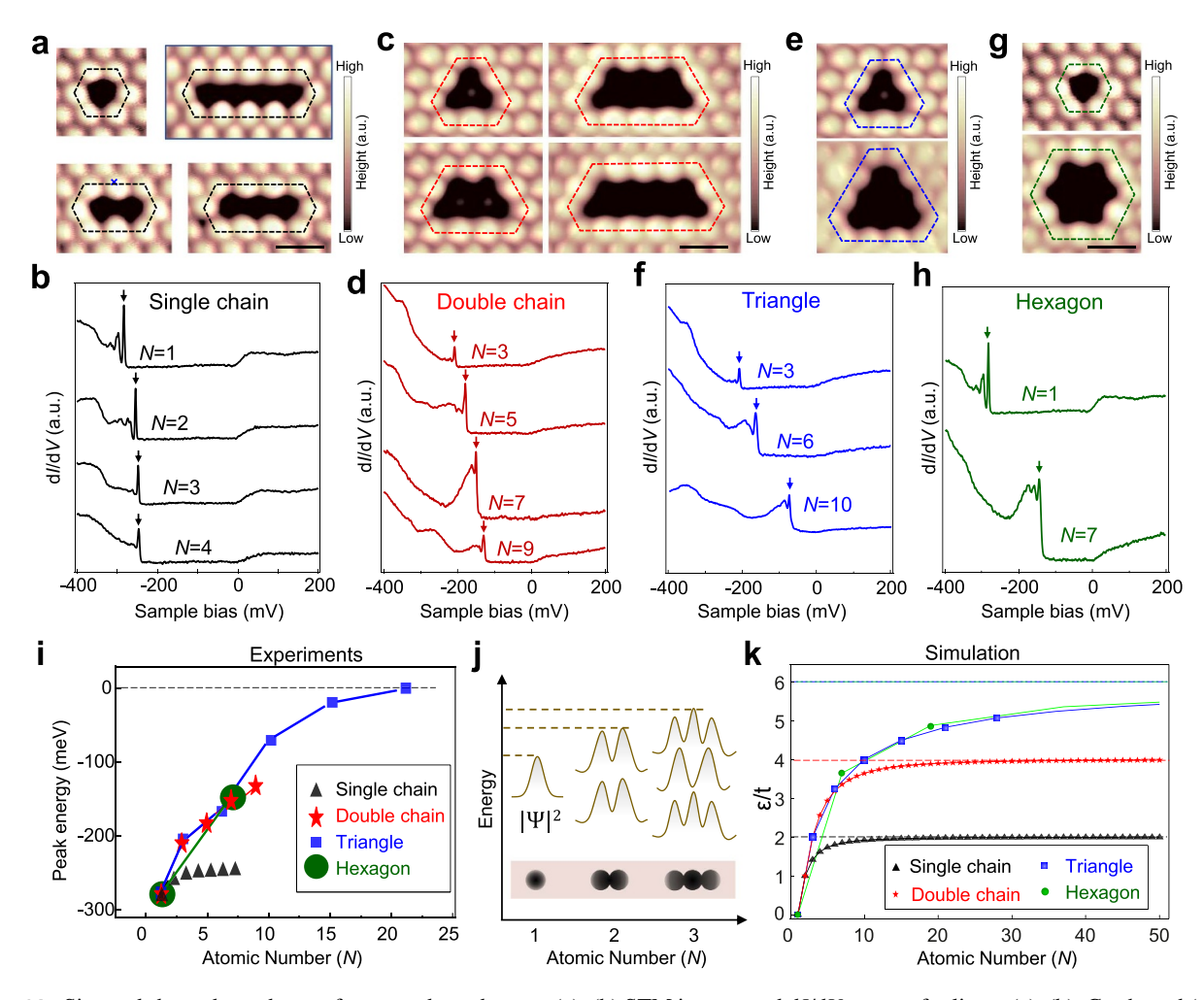


**Figure 14.** Size and shape dependence of vacancy bound states. (a)–(h) STM images and dI/dV spectra for linear (a), (b), C<sub>2</sub>-shaped (c), (d), triangular (e), (f), and hexagonal (g), (h) vacancies. Primary bound states are indicated by arrows in (b), (d), (f), (h). (i) Evolution of primary bound-state energies with vacancy size and shape, showing exponential dependence on symmetry. (j) Schematic of hybridization between vacancy bound states, where additional vacancies create higher-energy states. (k) Tight-binding calculations of bound-state evolution with atomic number, reproducing the experimental trend and illustrating quantum confinement effects. Reproduced from [73]. CC BY 4.0.

are the dominant native defects on both S- and Sn-terminated surfaces, give rise to a 'quantum cluster' structure. This term reflects the fact that a single dopant atom can generate a spatially confined cluster of localized electronic states, whose properties are highly sensitive to the local surface environment. Such clusters not only modify the surrounding electronic structure but also provide a controllable platform to study defect-induced quantum phenomena in Co<sub>3</sub>Sn<sub>2</sub>S<sub>2</sub>.

## 5.1. Atomic-scale identification of the oxygen-induced quantum clusters

On the Sn-terminated surface, STM topography reveals a slightly off-centered triangular shape intensity distribution (figures 15(a) and (b)), which locates at hollow site between three Sn atoms. The nc-AFM image shows a bright protrusion higher than typical Sn atoms in the center hollow site (figure 15(c)). Because the pristine Sn surface exhibits a flat-band peak near the Fermi energy, it is important to examine whether the dopant perturbs this feature. As shown in

figure 15(d), the peak shifts by roughly +5 meV relative to the dopant-free surface, indicating a local hole-doping effect.

On the S-terminated surface, the dopants reside slightly off-center from the S atomic lattice. STM topography reveals atomically sharp, hexagonally-symmetric protrusions, while nc-AFM imaging shows an atom 80 pm off center and 1.5 pm lower than neighboring S atoms (figures 15(e)–(g)). Spectroscopic measurements reveal pronounced in-gap states below  $-200 \, \mathrm{mV}$  (figure 15(h)). Spatial  $\mathrm{d}I/\mathrm{d}V$  maps at the energies of these localized states show distinct symmetry behaviors: at higher energies (e.g.  $-264 \, \mathrm{mV}$ ), the states exhibit a sixfold (C<sub>6</sub>) symmetric pattern centered on the dopant, indicating strong coupling to the underlying lattice symmetry; at lower energies (e.g.  $-362 \, \mathrm{mV}$ ), the symmetry reduces from C<sub>6</sub> to C<sub>2</sub>, suggesting energy-dependent orbital or structural anisotropy.

Atomic-resolution STEM combined with electron energy loss spectroscopy (EELS) confirms that the quantum clusters are originated from oxygen dopants occupy inequivalent sites within the  $\text{Co}_3\text{Sn}_2\text{S}_2$  lattice (figure 16). HAADF and annular

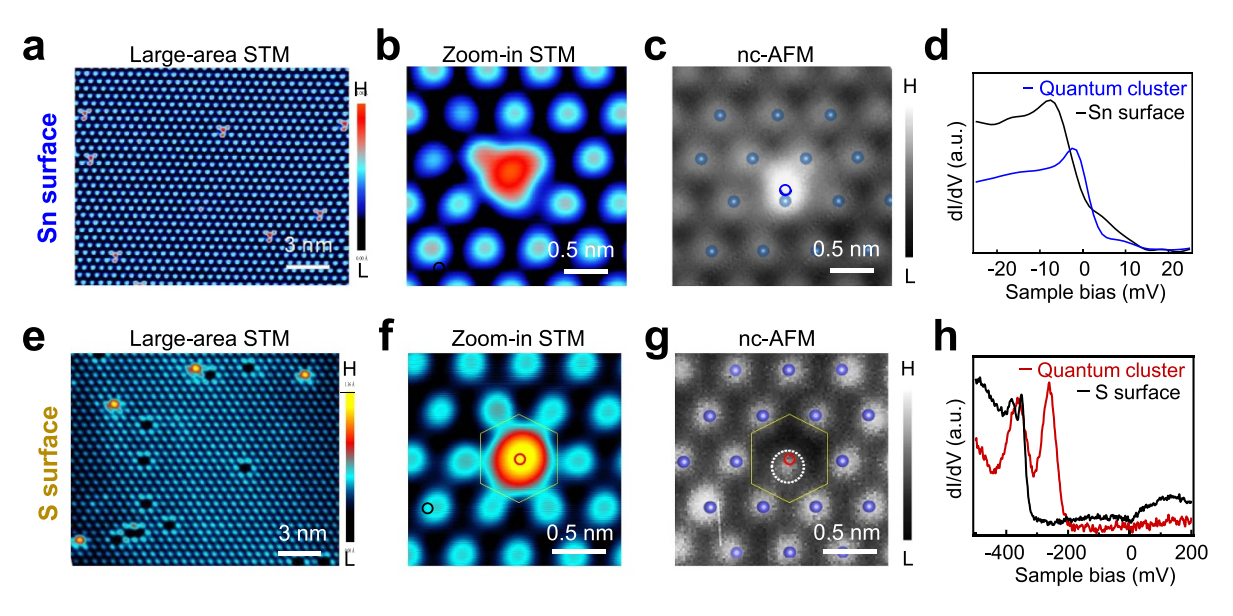


Figure 15. Surface characteristics of quantum clusters on Sn- and S- terminated surfaces. (a) Large-scale STM image of the Sn-terminated surface, where bright protrusions correspond to quantum clusters. (b) Zoom-in STM of a single cluster, showing asymmetric hybridization that yields a distorted triangular shape. (c) Nc-AFM image of the same cluster with atomic structure overlaid; blue circle marks the highest point of the dopant. (d) dI/dV spectra on (blue) and off (black) the cluster. (e) Large-scale STM of the S-terminated surface, showing randomly distributed quantum clusters as bright protrusions. (f) Zoom-in STM of a single cluster. (g) Nc-AFM of the same cluster with atomic overlay; white dashed circle marks the cluster; red circle marks the underlying S atom. (h) dI/dV spectra on (red) and off (black) the cluster, showing bound states at negative energies. Reproduced from [74]. Image stated to be in the public domain.

bright field (ABF) imaging along the [100] zone axis reveal two distinct configurations: one with the oxygen atom adjacent to the Sn plane and another near the S plane. In both cases, enhanced contrast in the ABF channel highlights the localized dopant site. EELS spectra taken at these regions show a clear oxygen K-edge onset at ~532 eV. For the Sn-adjacent configuration (figures 16(a)–(c)), the summed spectrum at the dopant site (green) displays the O K-edge in contrast to a reference spectrum from an O-free region (orange), with the differential spectrum (black) confirming a localized oxygen signal spatially correlated with the defect. The corresponding structural model depicts an O atom bonded in the vicinity of the Sn plane. For the S-adjacent configuration (figures 16(d)-(f)), EELS again shows the onset of oxygen-related features. The structural model places the O dopant between the S and Co<sub>3</sub>Sn atoms, giving rise to a different local chemical environment. Together, these observations demonstrate that oxygen is a dominant dopant species in Co<sub>3</sub>Sn<sub>2</sub>S<sub>2</sub>, occupying multiple inequivalent lattice sites and contributing to the diverse electronic signatures observed in STM.

#### 5.2. Interactions between neighboring quantum clusters

The spacing between pairs of oxygen-induced quantum clusters modulates their interactions on both S- and Sn-terminated surfaces. On the Sn termination, STM topographies reveal quantum clusters at varying separations (figure 17(a)), with sharp resonances near the Fermi level evolving systematically with distance, showing suppression of the doping-induced peak and recovery of the intrinsic flat-band feature (around -6 mV) as two quantum clusters approach each other

(figure 17(b)). When perpendicular magnetic fields ranging from -8 T to +8 T were applied, the peak near the Fermi level shifts linearly to higher energies with increasing field magnitude (figure 17(c)), consistent with a defect state exhibiting orbital magnetism and showing an anomalous Zeeman effect.

On the S-terminated surface, oxygen-induced quantum clusters display distinct behavior. The dI/dV spectra show that, as the quantum-clusters are brought into closer proximity, the defect-induced in-gap bound states broaden and undergo energy shifts (figure 17(e)), indicative of hybridization between their localized states. In contrast, dI/dV measurements performed under perpendicular magnetic fields ranging from -8 T to +8 T (figure 17(f)) reveal negligible Zeeman splitting or energy shifts, suggesting that these states are non-magnetic. This behavior contrasts with that of In impurities previously reported on the same surface termination [69].

These results demonstrate that oxygen-induced quantum clusters function as tunable, local quantum perturbations in the topological kagome magnet. Oxygen dopants give rise to spatially localized defect states, whose spectral, structural, and magnetic responses depend sensitively on their lattice positions. Moreover, their electronic properties can be modulated by external stimuli such as magnetic fields and inter-defect spacing, providing a versatile platform for the design and exploration of quantum phenomena in correlated and topological systems. Furthermore, it is feasible to control the oxygen dopant density during synthesis, thereby tuning the spatial arrangement and proximity of the quantum clusters. This allows selective modulation of the dominant interactions between clusters, providing a framework to understand how defect density and inter-cluster coupling can

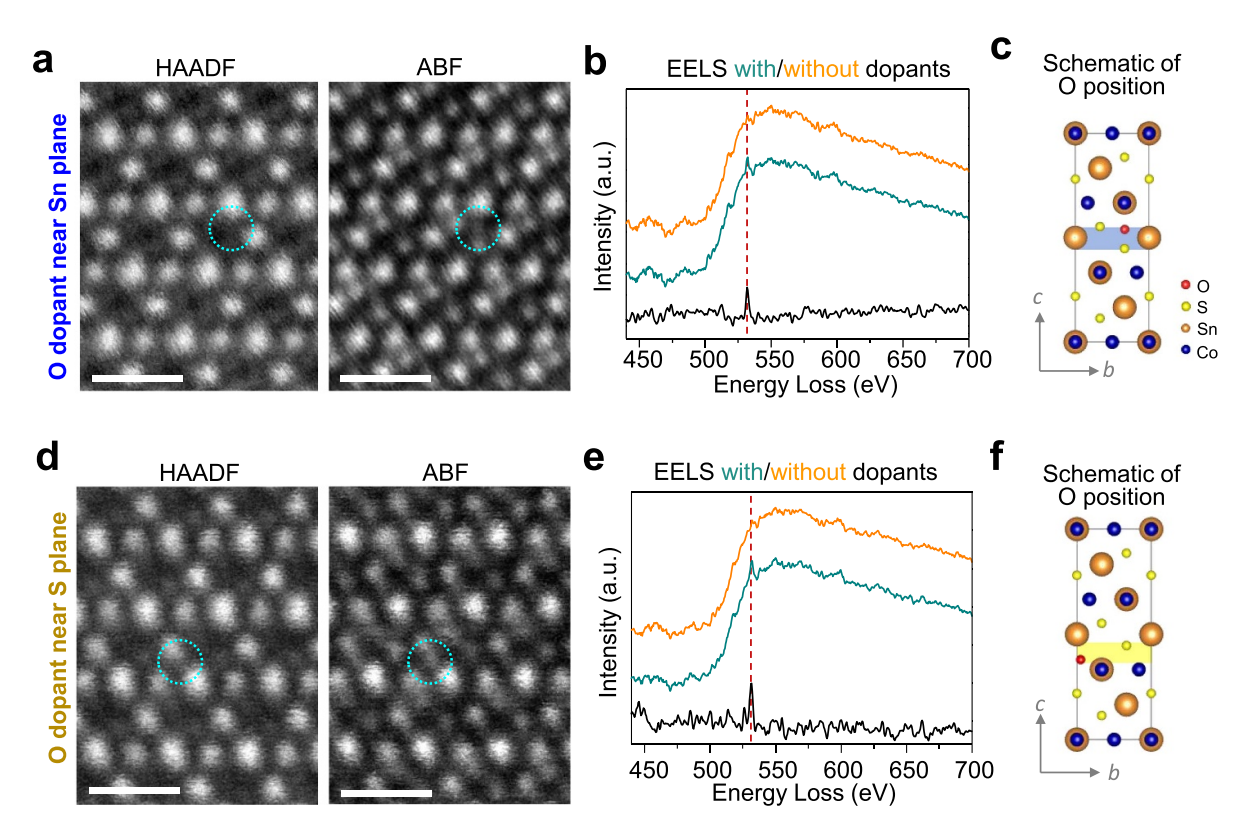


**Figure 16.** Cross-sectional STEM and EELS analysis of two types of oxygen-induced quantum clusters. (a) STEM high-angle annular dark field (HAADF, left) and inverted-contrast annular bright field (ABF, right) images of a dopant above the Sn plane (dashed circles) along the [100] zone axis. (b) EELS spectra of the Sn M-edge showing summed spectra with (green) and without (orange) oxygen signal at 532 eV; black line shows the difference. (c) Structural model with dopant above the Sn plane (red); Co: blue, Sn: golden, S: yellow. (d) STEM-HAADF (left) and ABF (right) of a dopant adjacent to the S plane (dashed circles). (e) EELS spectra of sites between pure Sn, Co<sub>3</sub>Sn, and pure Co columns with (green) and without (orange) O fine structure; black line shows the difference. (f) Structural model with dopant adjacent to the S plane (red). Scale bars: 0.5 nm. Reproduced from [74]. Image stated to be in the public domain.

influence emergent electronic and magnetic behavior in the bulk, thereby offering insights for tuning macroscopic properties based on atomic-scale control.

## 6. Kagome electronic states on surfaces: discovery and engineering

Besides the defect-related phenomena discussed in the last two sections, the cleaved S- and Sn-terminated surfaces of  $\text{Co}_3\text{Sn}_2\text{S}_2$  also host emergent electronic states that directly reflect the kagome symmetry of the underlying Co lattice. Recent studies have revealed that the triangular Sn and S surfaces can sustain a kagome electronic state arising from strong vertical p-d hybridization between the surface layers and the Co kagome layer underneath [70].

## 6.1. Kagome electronic states on surfaces yielded by vertical p-d hybridization

Revisiting the nc-AFM images of  $Co_3Sn_2S_2$  shown in figures 9 and 10, on the triangular Sn surface, the electronic states are spatially arranged in a kagome pattern, mirroring the kagome symmetry of Co atoms underneath. These kagome electronic states originate from Co d orbitals hybridized with in-plane p

orbitals of surface Sn and S atoms. Although the local density of states associated with Co d orbitals is significantly higher than that of Sn or S p orbitals, the d orbitals are spatially localized and screened by the p orbitals of the surface Sn or S atoms. Given the short-ranged nature of the measured repulsive interactions in nc-AFM imaging, the contribution of subsurface Co d orbitals is minimal. Consequently, the observed surface kagome electronic states are primarily attributed to hybridized states involving the surface Sn and S atoms with the Co d orbitals underneath, rather than directly to the Co d orbitals.

Theoretically local density of states projected (PLDOSs) onto the Sn-terminated surface (figure 18(a)) reveals a set of electronic states near the Fermi level ( $E_F$ ) that do not involve *s*-orbitals from surface Sn or S atoms. As shown in figure 18(b), these states arise from strong hybridization between surface Sn (blue) and subsurface S (green) *p* orbitals with underlying Co *d* orbitals (orange), as indicated by four distinct peaks (marked by red and blue dashed lines). The p-d hybridized states imprint the triangular electron density of the Co<sub>3</sub> trimers onto the surface Sn and S atoms. The squared of wavefunction norms of the occupied hybridized states ( $|\psi|^2$ , figure 18(e)) shows triangular contours at each Sn or S site, forming a kagome pattern with minimal density at the

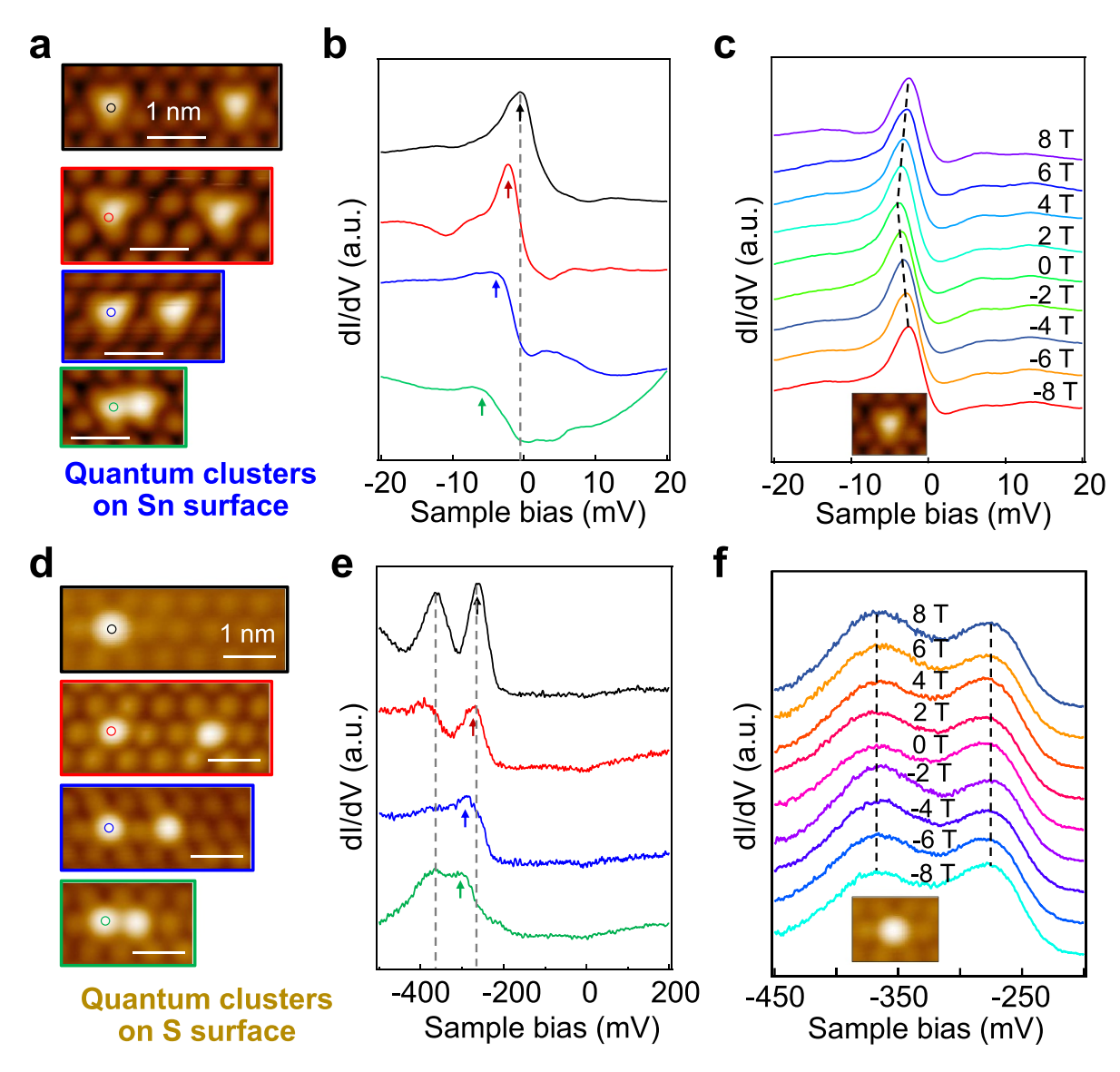


Figure 17. Interactions between neighboring quantum clusters on Sn and S surfaces. (a) Topographic STM images of two clusters on Sn surface with varying separation. (b) dI/dV spectra at the marked cluster in (a), showing evolution of states near the Fermi level. (c) dI/dV spectra of the peak near the Fermi energy under magnetic fields from -8 T to +8 T, showing a linear shift to higher energy. (d) Topographic STM images of two clusters on S surface with varying separation. (e) dI/dV spectra at the marked cluster in (d), showing evolution of defect states with cluster spacing. (f) dI/dV spectra of bound states under -8 T to +8 T, showing negligible magnetic response. Reproduced from [74]. Image stated to be in the public domain.

central Sn sites in the subsurface  $Co_3Sn$  layer. Lateral overlaps between these individual contours indicate further p–p hybridization, supported by the hybridized states residing at -0.25 and 0.37 eV (PLDOS peaks highlighted by red dashed lines in figure 18(b)). Thus, vertical p–d and lateral p–p hybridizations together transfer the kagome symmetry of the Co atoms in the subsurface  $Co_3Sn$  layer onto the Sn-terminated surface.

On the S surface, PLDOSs also show isolated states involving only surface S p and bulk Co d orbitals (figure 18(c)). A zoomed-in plot (figure 18(d)) highlights the vertical hybridization between the surface S p states and subsurface Co d states, indicated by blue dashed lines. This p-d hybridization imprints the triangular Co<sub>3</sub> electronic states onto the surface

S atoms, as shown by the  $|\psi|^2$  contour in figure 18(f). These contours form an incomplete kagome pattern on the S surface, since no electronic states appear on the red triangles (highlighted in figure 18(f)), which, together with the black triangles, form a complete kagome pattern. Consequently, the flat bands near the Fermi level observed on the Sn surface are absent on the S surface [60, 72].

## 6.2. Strategy for constructing a family of kagome electronic states on surfaces

The above findings indicate that the formation of kagome electronic states at surfaces relies on three prerequisites: (i) a honeycomb arrangement of surface and subsurface atoms,

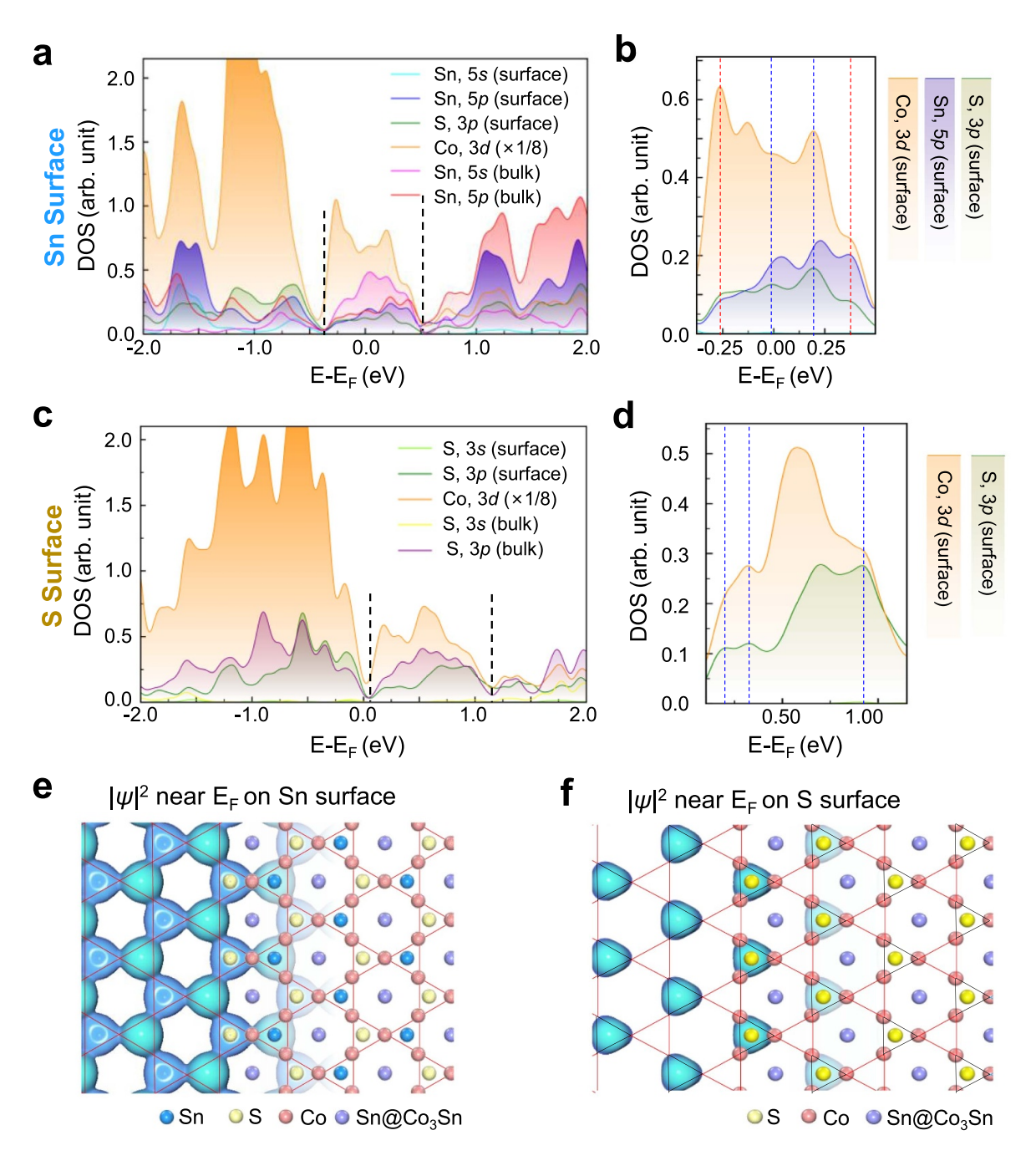


**Figure 18.** Vertical p-d and lateral p-p hybridizations on the Sn and S surfaces of  $Co_3Sn_2S_2$ . (a) Local density of states projected (PLDOSs) onto the Sn-terminated  $Co_3Sn_2S_2$  surface; black dashed lines at -0.38 and 0.50 eV indicate the energy range of isolated p-d hybridized states. (b) PLDOSs of the top three atomic layers of the Sn-terminated surface; blue and red dashed lines denote vertical p-d hybridization with the Co kagome lattice, with red lines also indicating lateral hybridization between surface Sn and subsurface S p states. (c) PLDOSs of the S-terminated  $Co_3Sn_2S_2$  surface; isolated p-d hybridized states are observable between 0.12 and 1.16 eV (marked by black dashed lines). (d) PLDOSs of the top three layers of the S-terminated surface; blue dashed lines indicate vertical p-d hybridization of S p states with Co d states underneath. (e) Wavefunction norm square contours of hybridized states on the Sn surface (integrated from -0.38 to 0.50 eV) decorated with a top view of atomic structures of surface Sn, subsurface S, and  $Co_3Sn$  atoms; red solid lines highlight kagome symmetry. (f) Wavefunction norm square contours of hybridized states on the S surface (integrated from 0.12 to 1.16 eV) decorated with a top view of atomic structures of surface S and  $Co_3Sn$  atoms; red solid lines highlight triangular symmetry. Reproduced from [70]. CC BY 4.0.

(ii) vertical hybridization of their in-plane orbitals with both sublattices of the underlying kagome lattice, and (iii) lateral hybridization among the vertically hybridized states to produce a kagome-symmetric electronic structure, as illustrated in figure 19. The Sn-terminated surface of Co<sub>3</sub>Sn<sub>2</sub>S<sub>2</sub> fulfills

these criteria, with surface Sn and subsurface S atoms (0.56 Å below) occupying opposite sublattices of the kagome Co lattice underneath. By contrast, the S-terminated surface fails to meet condition (i) and therefore supports only the formation of an incomplete kagome electronic state (right panel, figure 19).

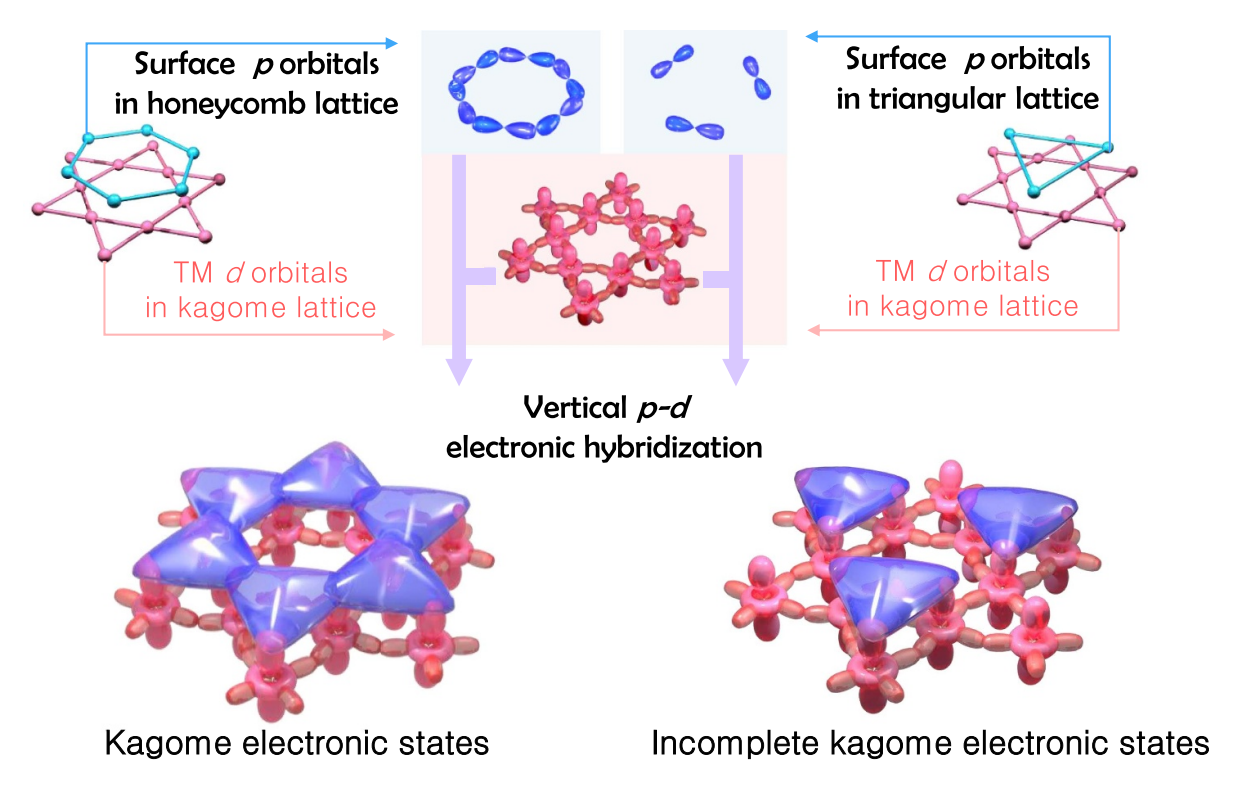


**Figure 19.** Schematic on the vertical p–d hybridization between d states of  $Co_3$  triangles and p states of surface atoms. A complete kagome electronic state emerges when surface and subsurface atoms occupy complementary sublattices (left panel), whereas an incomplete kagome electronic state arises when this lattice symmetry is not satisfied (right panel). Reproduced from [70]. CC BY 4.0.

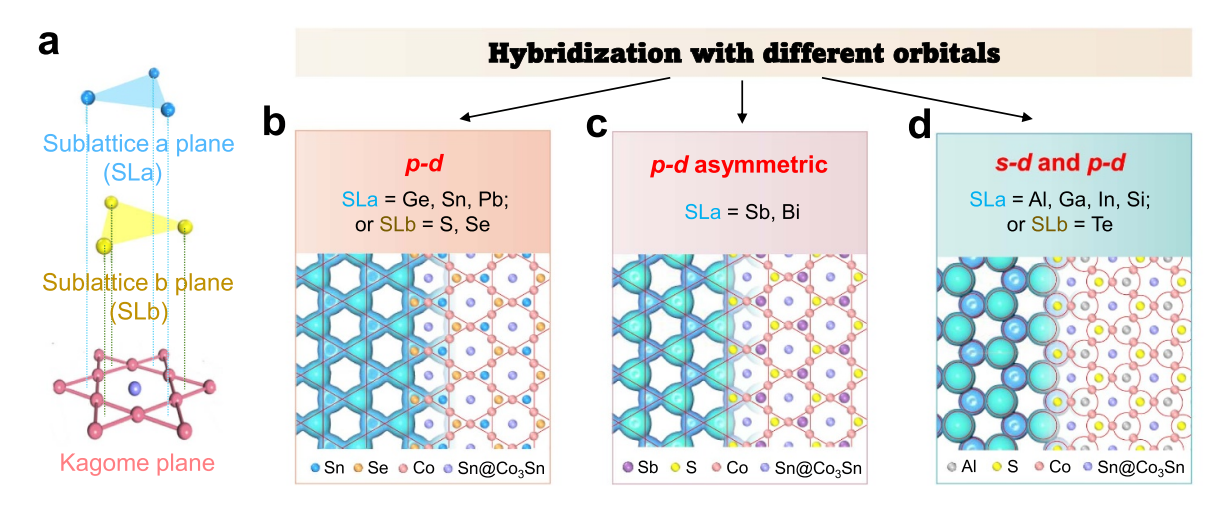


**Figure 20.** Theoretical construction of kagome metal family by depositing or substituting atoms on  $Co_3Sn_2S_2$  surfaces. (a) Schematic of the surface planes that sits on top of sublattice a (blue, plane SLa) and sublattice b (yellow, plane SLb) of the kagome plane (red). (b)–(d) Wavefunction norm square contours of hybridized states showing p–d hybridization, asymmetric p–d hybridization, and combined s–d and p–d hybridization, respectively; corresponding deposited or substituted atoms are indicated at the upper portion of each panel. Reproduced from [70]. CC BY 4.0.

However, depositing hetero- or homo-atoms onto the complementary sublattice (sublattice plane **a**, SLa; figure 20(a)) restores the missing component, enabling the realization of kagome electronic states on the S-terminated surface with tunable properties. Additionally, substituting S atoms in sublattice plane **b** (SLb, figure 20(a)) with Se or Te during bulk crystal growth provides another pathway to engineer a broader variety of kagome electronic states.

DFT calculations confirm that modifying the SLa and SLb planes yields diverse surface hybridizations. When SLa=Ge, Sn, or Pb and SLb=S or Se, vertical p-d hybridization persists, forming isolated kagome-like states near  $E_F$  (e.g. figure 20(b) for SLa=Sn, SLb=Se). A breathing kagome symmetry is achieved by unbalancing the hybridization between SLa and SLb, e.g. with heavier SLa atoms like Sb or Bi (figure 20(c)). For SLa=Al, Ga, In, or Si or SLb=Te, s orbitals

also participate in hybridization near  $E_F$ , resulting in spherical  $|\psi|^2$  contours and weakened kagome features (figure 20(d)). These findings highlight the S-terminated surface as a platform for engineered kagome electronic states.

This strategy can be readily extended to kagome materials sharing the structural features of Co<sub>3</sub>Sn<sub>2</sub>S<sub>2</sub>, where the interplay of lattice geometry, SOC, and surface termination also governs the formation of kagome electronic states at surfaces. By selectively substituting atoms or depositing adatoms, one can systematically tune the electronic, magnetic, and topological properties of these surfaces. This tunability opens up new opportunities for designing functional quantum materials and devices through tailored surface states in kagome lattices.

#### 7. Conclusion and perspectives

This review presents advances in surface studies of Co<sub>3</sub>Sn<sub>2</sub>S<sub>2</sub> by STM and nc-AFM, which provide atomic-scale insights into surface identification, defect manipulation, and engineering of electronic and magnetic states, elucidating the interplay of electronic band topology, magnetism, and electron correlations in kagome-lattice Weyl semimetal Co<sub>3</sub>Sn<sub>2</sub>S<sub>2</sub>. The resulting understanding consolidates the role of Co<sub>3</sub>Sn<sub>2</sub>S<sub>2</sub> as a model platform for correlated topological phenomena and opens avenues for future electronic and spintronic applications. The key insights of this review can be summarized as follows:

- (1) The synthesis of ultra-high-quality Co<sub>3</sub>Sn<sub>2</sub>S<sub>2</sub> single crystals provides a crucial basis for their potential applications in electronic and spintronic devices. Using an iterative-CVT method, researchers have achieved largearea stoichiometric crystals with exceptional crystallinity, enabling direct observations of the flat band and significantly enhanced anomalous Hall conductivity.
- (2) Surface identifications in Co<sub>3</sub>Sn<sub>2</sub>S<sub>2</sub> have been unambiguously established through atomic-scale studies combining work function measurements, bond-resolved nc-AFM imaging, and short-range force spectroscopy. These identifications resolve the long-standing debate on the atomic details of cleaved surfaces and establish a solid foundation for further surface-focused investigations.
- (3) Discoveries of SOP at S vacancies, oxygen-induced quantum clusters, and kagome electronic states on the surfaces reveal diverse and tunable properties of Co<sub>3</sub>Sn<sub>2</sub>S<sub>2</sub> surfaces. These findings demonstrate how atomic-scale perturbations interact with the underlying topological quantum states, giving rise to diverse emergent electronic and magnetic behaviors.
- (4) The physical properties of SOP, oxygen-induced quantum clusters, and surface kagome electronic states can be engineered through both on-surface atomic manipulation and controlled crystal growth. This tunability offers broad opportunities for scalable control of electronic and magnetic behaviors, and thereby facilitating the design and exploration of novel quantum phenomena in kagomelattice materials.

Looking forward, Co<sub>3</sub>Sn<sub>2</sub>S<sub>2</sub> is well positioned to remain a model system for investigating fundamental physics of correlated topological states. The combination of its tunable surface and bulk properties with modern approaches to defect engineering and atomic-scale perturbations provides a powerful pathway toward exploring new electronic and magnetic functionalities. Future studies of Co<sub>3</sub>Sn<sub>2</sub>S<sub>2</sub> will benefit from further advances in ultra-high quality crystal growth and engineering of novel quantum structures.

The iterative-CVT method has already enabled the synthesis of large, stoichiometric crystals with exceptional quality [71], but refining growth techniques to suppress unintentional impurities, realize controllable doping, and stabilize the material against surface degradation will be crucial for enabling more complex experiments. The high-quality crystals also provide a solid foundation for the future applications in electronic and spintronic devices. In particular, achieving stable few-layer crystals [119–121] and well-defined interfaces may open opportunities to integrate Co<sub>3</sub>Sn<sub>2</sub>S<sub>2</sub> with other quantum materials, such as superconductors or two-dimensional magnets, for creating heterostructures that host exotic emergent states.

High-quality crystals provide a foundation for discovering and engineering novel physical properties. Combined high-quality crystal with complementary *in situ* techniques, such as atomic manipulation using STM tips [122] and molecular beam epitaxy for controlled foreign-atom deposition, researcher can deliberately create atomic scale quantum states and control of their interactions within these materials, thereby enabling systematic studies of defect- and dopant-engineered quantum phenomena.

Another promising direction lies in the controlled realization of kagome electronic states at surfaces. Atomic deposition offers a route to construct artificial kagome states with tunable electronic bandstructures [70]. Varying the deposited or substituted atomic species enables versatile tuning of electronic band structures, flat-band features, and orbital magnetism. This level of control could allow the design of artificial lattices with tailored topological electronic properties, providing new platforms to explore correlated flat-band physics, interaction-driven topological phases, or even exotic superconductivity in kagome materials.

#### Data availability statement

All data that support the findings of this study are included within the article (and any supplementary files).

#### Acknowledgment

We thank Ziqiang Wang, Binghai Yan, Hechang Lei, Enke Liu, Xianggang Qiu, Wu Zhou, Yu-Yang Zhang, Xianghua Kong, Hengxin Tan, Wei Jiang, Feng Liu, and Claudia Felser for helpful discussions and valuable suggestion. We acknowledge the financial support from the National Natural Science Foundation of China (Grants Nos. 62488201, 92463307, 92477205, and 52461160327), the

National Key Research and Development Program of China (Grants Nos. 2024YFA1207700, 2022YFA1204100, and 2023YFA1406500), the Innovation Program of Quantum Science and Technology (2021ZD0302700), the CAS Project for Young Scientists in Basic Research (YSBR-003), and the CAS Superconducting Research Project (SCZX-0101).

#### **ORCID iDs**

Li Huang © 0000-0002-5964-7090 Qi Zheng © 0000-0002-8946-536X Lan Chen © 0000-0003-4426-9944 Hui Chen © 0000-0002-3369-8113 Haitao Yang © 0000-0003-4304-9835 Wei Ji © 0000-0001-5249-6624 Hong-Jun Gao © 0000-0002-2088-0522

#### References

- [1] Koshibae W and Maekawa S 2003 Electronic state of a CoO<sub>2</sub> layer with hexagonal structure: a kagome lattice structure in a triangular lattice *Phys. Rev. Lett.* 91 257003
- [2] Depenbrock S, McCulloch I P and Schollwoeck U 2012 Nature of the spin-liquid ground state of the S=1/2 Heisenberg model on the kagome lattice *Phys. Rev. Lett.* 109 067201
- [3] Han T-H, Helton J S, Chu S, Nocera D G, Rodriguez-Rivera J A, Broholm C and Lee Y S 2012 Fractionalized excitations in the spin-liquid state of a kagome-lattice antiferromagnet *Nature* 492 406–10
- [4] Chisnell R, Helton J S, Freedman D E, Singh D K, Bewley R I, Nocera D G and Lee Y S 2015 Topological magnon bands in a kagome lattice ferromagnet *Phys. Rev.* Lett. 115 147201
- [5] Hutter A, Wootton J R and Loss D 2015 Parafermions in a kagome lattice of qubits for topological quantum computation *Phys. Rev. X* 5 041040
- [6] Ezawa M 2018 Higher-order topological insulators and semimetals on the breathing kagome and pyrochlore lattices *Phys. Rev. Lett.* 120 026801
- [7] Li Z et al 2018 Realization of flat band with possible nontrivial topology in electronic kagome lattice Sci. Adv. 4 eaau4511
- [8] Lin Z et al 2018 Flatbands and emergent ferromagnetic ordering in Fe<sub>3</sub>Sn<sub>2</sub> kagome lattices Phys. Rev. Lett. 121 096401
- [9] Sethi G, Zhou Y, Zhu L, Yang L and Liu F 2021 Flat-band-enabled triplet excitonic insulator in a diatomic kagome lattice *Phys. Rev. Lett.* 126 196403
- [10] Sethi G, Cuma M and Liu F 2023 Excitonic condensate in flat valence and conduction bands of opposite chirality *Phys. Rev. Lett.* 130 186401
- [11] Yin J-X *et al* 2018 Giant and anisotropic many-body spin–orbit tunability in a strongly correlated kagome magnet *Nature* **562** 91–95
- [12] Ortiz B R et al 2019 New kagome prototype materials: discovery of KV<sub>3</sub>Sb<sub>5</sub>, RbV<sub>3</sub>Sb<sub>5</sub>, and CsV<sub>3</sub>Sb<sub>5</sub> Phys. Rev. Mater. 3 094407
- [13] Chen H *et al* 2021 Roton pair density wave in a strong-coupling kagome superconductor *Nature* **599** 222–8
- [14] Jiang Y-X et al 2021 Unconventional chiral charge order in kagome superconductor KV3Sb5 Nat. Mater. 20 1353–7

- [15] Tan H, Liu Y, Wang Z and Yan B 2021 Charge density waves and electronic properties of superconducting kagome metals *Phys. Rev. Lett.* 127 046401
- [16] Yin Q, Tu Z, Gong C, Tian S and Lei H 2021 Structures and physical properties of V-based kagome metals CsV<sub>8</sub>Sb<sub>12</sub> Chin. Phys. Lett. 38 127401
- [17] Xiang Y, Li Q, Li Y, Xie W, Yang H, Wang Z, Yao Y and Wen H-H 2021 Twofold symmetry of *c*-axis resistivity in topological kagome superconductor CsV3Sb5 with in-plane rotating magnetic field *Nat. Commun.* 12 6727
- [18] Zhao H, Li H, Ortiz B R, Teicher S M L, Park T, Ye M, Wang Z, Balents L, Wilson S D and Zeljkovic I 2021 Cascade of correlated electron states in the kagome superconductor CsV<sub>3</sub>Sb<sub>5</sub> Nature 599 216–21
- [19] Yang Y et al 2021 Discovery of two families of VSb-based compounds with V-kagome lattice Chin. Phys. Lett. 38 127102
- [20] Neupert T, Denner M M, Yin J-X, Thomale R and Hasan M Z 2022 Charge order and superconductivity in kagome materials *Nat. Phys.* 18 137–43
- [21] Yin J-X, Lian B and Hasan M Z 2022 Topological kagome magnets and superconductors *Nature* 612 647–57
- [22] Luo H et al 2022 Electronic nature of charge density wave and electron-phonon coupling in kagome superconductor KV3Sb5 Nat. Commun. 13 273
- [23] Nie L et al 2022 Charge-density-wave-driven electronic nematicity in a kagome superconductor Nature 604 59–64
- [24] Broyles C, Graf D, Yang H, Dong X, Gao H and Ran S 2022 Effect of the interlayer ordering on the Fermi surface of kagome superconductor CsV<sub>3</sub>Sb<sub>5</sub> revealed by quantum oscillations *Phys. Rev. Lett.* 129 157001
- [25] Yang H et al 2022 Titanium doped kagome superconductor  $CsV_{3-x}Ti_xSb_5$  and two distinct phases Sci. Bull. 67 2176–85
- [26] Wang Y, Wu H, McCandless G T, Chan J Y and Ali M N 2023 Quantum states and intertwining phases in kagome materials *Nat. Rev. Phys.* 5 635–58
- [27] Hu Y et al 2023 Non-trivial band topology and orbital-selective electronic nematicity in a titanium-based kagome superconductor Nat. Phys. 19 1827–33
- [28] Chowdhury N, Khan K I A, Bangar H, Gupta P, Yadav R S, Agarwal R, Kumar A and Muduli P K 2023 Kagome magnets: the emerging materials for spintronic memories *Proc. Natl Acad. Sci. A* 93 477–95
- [29] Guguchia Z et al 2023 Tunable unconventional kagome superconductivity in charge ordered RbV<sub>3</sub>Sb<sub>5</sub> and KV<sub>3</sub>Sb<sub>5</sub> Nat. Commun. 14 153
- [30] Luo Y et al 2023 A unique van Hove singularity in kagome superconductor CsV<sub>3-x</sub>Ta<sub>x</sub>Sb<sub>5</sub> with enhanced superconductivity Nat. Commun. 14 3819
- [31] Yang J *et al* 2023 Observation of flat band, Dirac nodal lines and topological surface states in Kagome superconductor CsTi<sub>3</sub>Bi<sub>5</sub> *Nat. Commun.* **14** 4089
- [32] Wilson S D and Ortiz B R 2024 AV<sub>3</sub>Sb<sub>5</sub> kagome superconductors *Nat. Rev. Mater.* **9** 420–32
- [33] Candelora C, Li H, Xu M, Ortiz B R, Salinas A C, Cheng S, LaFleur A, Wang Z, Wilson S D and Zeljkovic I 2024 Quantifying magnetic field driven lattice distortions in kagome metals at the femtometer scale using scanning tunneling microscopy *Phys. Rev. B* 109 155121
- [34] Li H *et al* 2024 Spin Berry curvature-enhanced orbital Zeeman effect in a kagome metal *Nat. Phys.* **20** 1103–9
- [35] Liu G, Yang T, Jiang Y-X, Hossain S, Deng H, Hasan M Z and Yin J-X 2024 Perspective: imaging atomic step geometry to determine surface terminations of kagome materials and beyond *Quantum Frontiers* 3 19
- [36] Xing Y et al 2024 Optical manipulation of the charge-density-wave state in RbV<sub>3</sub>Sb<sub>5</sub> Nature **631** 60–66

- [37] Hu B et al 2024 Evidence of a distinct collective mode in kagome superconductors Nat. Commun. 15 6109
- [38] Huang Z et al 2024 Tunable vortex bound states in multiband CsV<sub>3</sub>Sb<sub>5</sub>-derived kagome superconductors Sci. Bull. 69 885–92
- [39] Yang H et al 2024 Superconductivity and nematic order in a new titanium-based kagome metal CsTi<sub>3</sub>Bi<sub>5</sub> without charge density wave order Nat. Commun. 15 9626
- [40] Huang Z et al 2025 Revealing the orbital origins of exotic electronic states with Ti substitution in kagome superconductor CsV<sub>3</sub>Sb<sub>5</sub> Phys. Rev. Lett. 134 056001
- [41] Lv S et al 2025 Field-induced butterfly-like anisotropic magnetoresistance in a kagome semimetal Co<sub>3</sub>In<sub>2</sub>S<sub>2</sub> Adv. Funct. Mater. 35 2412876
- [42] Yin J-X et al 2020 Quantum-limit Chern topological magnetism in TbMn<sub>6</sub>Sn<sub>6</sub> Nature **583** 533–6
- [43] Zhang S S et al 2020 Many-body resonance in a correlated topological kagome antiferromagnet Phys. Rev. Lett. 125 046401
- [44] Zhou H et al 2020 Enhanced anomalous Hall effect in the magnetic topological semimetal Co<sub>3</sub>Sn<sub>2-x</sub>In<sub>x</sub>S<sub>2</sub> Phys. Rev. B 101 12
- [45] Hasan M Z, Chang G, Belopolski I, Bian G, Xu S-Y and Yin J-X 2021 Weyl, Dirac and high-fold chiral fermions in topological quantum matter *Nat. Rev. Mater.* 6 784–803
- [46] Yin J-X, Pan S H and Zahid Hasan M 2021 Probing topological quantum matter with scanning tunnelling microscopy Nat. Rev. Phys. 3 249–63
- [47] Armitage N P, Mele E J and Vishwanath A 2018 Weyl and Dirac semimetals in three-dimensional solids *Rev. Mod. Phys.* 90 015001
- [48] Ren Z et al 2022 Plethora of tunable Weyl fermions in kagome magnet Fe<sub>3</sub>Sn<sub>2</sub> thin films npj Quantum. Mater. 7 109
- [49] Zhu M et al 2024 Two-dimensional ultrathin Fe<sub>3</sub>Sn<sub>2</sub> kagome metal with defect-dependent magnetic property Nano Lett. 24 7483–90
- [50] Liu J and Balents L 2017 Anomalous hall effect and topological defects in antiferromagnetic Weyl semimetals: Mn<sub>3</sub>Sn/Ge *Phys. Rev. Lett.* 119 087202
- [51] Yang H, Sun Y, Zhang Y, Shi W-J, Parkin S S P and Yan B 2017 Topological Weyl semimetals in the chiral antiferromagnetic materials Mn<sub>3</sub>Ge and Mn<sub>3</sub>Sn New J. Phys. 19 015008
- [52] Ye L *et al* 2018 Massive Dirac fermions in a ferromagnetic kagome metal *Nature* 555 638–24
- [53] Nakatsuji S, Kiyohara N and Higo T 2015 Large anomalous Hall effect in a non-collinear antiferromagnet at room temperature *Nature* 527 212–5
- [54] Liu D F *et al* 2019 Magnetic Weyl semimetal phase in a kagome crystal *Science* **365** 1282–5
- [55] Liu E et al 2018 Giant anomalous Hall effect in a ferromagnetic kagome-lattice semimetal Nat. Phys. 14 1125–31
- [56] Wang Q, Xu Y, Lou R, Liu Z, Li M, Huang Y, Shen D, Weng H, Wang S and Lei H 2018 Large intrinsic anomalous Hall effect in half-metallic ferromagnet Co<sub>3</sub>Sn<sub>2</sub>S<sub>2</sub> with magnetic Weyl fermions *Nat. Commun.* 9 3681
- [57] Guin S N et al 2019 Zero-field Nernst effect in a ferromagnetic kagome-lattice Weyl-semimetal Co<sub>3</sub>Sn<sub>2</sub>S<sub>2</sub> Adv. Mater. 31 1806622
- [58] Jiao L, Xu Q, Cheon Y, Sun Y, Felser C, Liu E and Wirth S 2019 Signatures for half-metallicity and nontrivial surface states in the kagome lattice Weyl semimetal Co<sub>3</sub>Sn<sub>2</sub>S<sub>2</sub> Phys. Rev. B 99 245158
- [59] Yin J-X et al 2019 Negative flat band magnetism in a spin-orbit-coupled correlated kagome magnet Nat. Phys. 15 443–8

- [60] Morali N, Batabyal R, Nag P K, Liu E, Xu Q, Sun Y, Yan B, Felser C, Avraham N and Beidenkopf H 2019 Fermi-arc diversity on surface terminations of the magnetic Weyl semimetal Co<sub>3</sub>Sn<sub>2</sub>S<sub>2</sub> Science 365 1286–91
- [61] Shen J et al 2020 33% giant anomalous Hall current driven by both intrinsic and extrinsic contributions in magnetic Weyl semimetal Co<sub>3</sub>Sn<sub>2</sub>S<sub>2</sub> Adv. Funct. Mater. 30 2000830
- [62] Howard S et al 2021 Evidence for one-dimensional chiral edge states in a magnetic Weyl semimetal Co<sub>3</sub>Sn<sub>2</sub>S<sub>2</sub> Nat. Commun. 12 4269
- [63] Wang Q et al 2023 Magnetism modulation in Co<sub>3</sub>Sn<sub>2</sub>S<sub>2</sub> by current-assisted domain wall motion Nat. Electron. 6 119–25
- [64] Zhao J, Jiang B, Zhang S, Wang L, Liu E, Li Z and Wu X 2023 Magnetoresistance signature of two-dimensional electronic states in Co<sub>3</sub>Sn<sub>2</sub>S<sub>2</sub> Phys. Rev. B 107 085203
- [65] Liu J et al 2025 Unusually high occupation of Co 3d state in magnetic Weyl semimetal Co<sub>3</sub>Sn<sub>2</sub>S<sub>2</sub> ACS Nano 19 8561–70
- [66] Yang J et al 2025 Modulation of the anomalous Hall angle in a magnetic topological semimetal *Nat. Electron*. 8 386–93
- [67] Liu E and Zhang S 2019 Topologically enhanced zero-field transverse Nernstthermoelectric effect in magnetic topological semimetals Sci. Sin. Phys. Mech. Astron. 49 127001
- [68] Tanaka M et al 2020 Topological kagome magnet Co<sub>3</sub>Sn<sub>2</sub>S<sub>2</sub> thin flakes with high electron mobility and large anomalous Hall effect Nano Lett. 20 7476–81
- [69] Yin J-X *et al* 2020 Spin-orbit quantum impurity in a topological magnet *Nat. Commun.* **11** 4415
- [70] Huang L et al 2023 Discovery and construction of surface kagome electronic states induced by p-d electronic hybridization in Co<sub>3</sub>Sn<sub>2</sub>S<sub>2</sub> Nat. Commun. 14 5230
- [71] Lv S et al 2025 Bipolarity induced gigantic intrinsic anomalous Hall effect in iterative-grown kagome semimetal Co<sub>3</sub>Sn<sub>2</sub>S<sub>2</sub> crystals Adv. Funct. Mater. e10587
- [72] Xing Y et al 2020 Localized spin-orbit polaron in magnetic Weyl semimetal Co<sub>3</sub>Sn<sub>2</sub>S<sub>2</sub> Nat. Commun. 11 5613
- [73] Chen H et al 2024 Atomically precise engineering of spin–orbit polarons in a kagome magnetic Weyl semimetal Nat. Commun. 15 2301
- [74] Xing Y, Chen H, Huang L, Guzman R, Zheng Q, Lv S, Shi J, Yang H, Zhou W and Gao H-J 2025 Intrinsic quantum clusters in kagome Weyl semimetal Co<sub>3</sub>Sn<sub>2</sub>S<sub>2</sub> (arXiv:2509.11230)
- [75] Lei J, Xie Y, Kutana A, Bets K V and Yakobson B I 2022 Salt-assisted MoS<sub>2</sub> growth: molecular mechanisms from the first principles J. Am. Chem. Soc. 144 7497–503
- [76] Zhou X, He S, Liu G, Zhao L, Yu L and Zhang W 2018 New developments in laser-based photoemission spectroscopy and its scientific applications: a key issues review *Rep. Prog. Phys.* 81 062101
- [77] Kim D and Liu F 2023 Realization of flat bands by lattice intercalation in kagome metals *Phys. Rev. B* 107 205130
- [78] Busch G A and Kern R 1960 Semiconducting properties of gray tin *Solid State Phys.* 11 1–40
- [79] Haq A U, Askari S, McLister A, Rawlinson S, Davis J, Chakrabarti S, Svrcek V, Maguire P, Papakonstantinou P and Mariotti D 2019 Size-dependent stability of ultra-small α-/β-phase tin nanocrystals synthesized by microplasma Nat. Commun. 10 817
- [80] Hörmann N G, Gross A, Rohrer J and Kaghazchi P 2015 Stabilization of the γ-Sn phase in tin nanoparticles and nanowires Appl. Phys. Lett. 107 123101
- [81] Sabet S and Kaghazchi P 2014 Communication: nanosize-induced restructuring of Sn nanoparticles J. Chem. Phys. 140 191102

- [82] Liu G, Song W, Neupert T, Hasan M Z, Deng H and Yin J-X 2025 Atomic perspective on the topological magnetism in kagome metal Co<sub>3</sub>Sn<sub>2</sub>S<sub>2</sub> Quantum Frontiers 4 12
- [83] Giessibl F J 1997 Forces and frequency shifts in atomic-resolution dynamic-force microscopy *Phys. Rev. B* 56 16010–5
- [84] Sader J E and Jarvis S P 2004 Accurate formulas for interaction force and energy in frequency modulation force spectroscopy Appl. Phys. Lett. 84 1801–3
- [85] Sader J E, Uchihashi T, Higgins M J, Farrell A, Nakayama Y and Jarvis S P 2005 Quantitative force measurements using frequency modulation atomic force microscopy—theoretical foundations *Nanotechnology* 16 S94-S101
- [86] Nonnenmacher M, O'Boyle M P and Wickramasinghe H K 1991 Kelvin probe force microscopy Appl. Phys. Lett. 58 2921–3
- [87] Giessibl F J 2000 Atomic resolution on Si(111)-(7×7) by noncontact atomic force microscopy with a force sensor based on a quartz tuning fork *Appl. Phys. Lett.* 76 1470-2
- [88] Giessibl F J 2003 Advances in atomic force microscopy Rev. Mod. Phys. 75 949–83
- [89] Gross L, Mohn F, Moll N, Liljeroth P and Meyer G 2009 The chemical structure of a molecule resolved by atomic force microscopy *Science* 325 1110–4
- [90] Gross L, Mohn F, Moll N, Schuler B, Criado A, Guitián E, Peña D, Gourdon A and Meyer G 2012 Bond-order discrimination by atomic force microscopy *Science* 337 1326–9
- [91] Riss A et al 2016 Imaging single-molecule reaction intermediates stabilized by surface dissipation and entropy Nat. Chem. 8 678–83
- [92] Pavliček N, Mistry A, Majzik Z, Moll N, Meyer G, Fox D J and Gross L 2017 Synthesis and characterization of triangulene Nat. Nanotechnol. 12 308–11
- [93] Kaiser K, Scriven L M, Schulz F, Gawel P, Gross L and Anderson H L 2019 An sp-hybridized molecular carbon allotrope, cyclo 18 carbon *Science* 365 1299–301
- [94] Cao Y *et al* 2018 Tuning the morphology of chevron-type graphene nanoribbons by choice of annealing temperature *Nano Res.* 11 6190–6
- [95] Fu Y *et al* 2020 On-surface synthesis of NBN-doped zigzag-edged graphene nanoribbons *Angew. Chem., Int. Ed.* **59** 8873–9
- [96] Huan Y, Yun C, Yixuan G, Yubin F, Li H, Junzhi L, Xinliang F, Shixuan D and Hong-Jun G 2021 NBN-doped nanographene embedded with five- and seven-membered rings on Au(111) surface *Chin. Phys. B* 30 056802
- [97] Gao Y et al 2022 Selective activation of four quasi-equivalent
   C-H bonds yields N-doped graphene nanoribbons with partial corannulene motifs Nat. Commun.
   13 6146
- [98] Zheng Q, Huang L, Bao D, Wu R, Li Y, Lin X, Du S and Gao H-J 2022 Substrate tuned reconstructed polymerization of naphthalocyanine on Ag(110) Chin. Phys. B 31 018202
- [99] Fu X et al 2025 Building spin-1/2 antiferromagnetic Heisenberg chains with diaza-nanographenes Nat. Synth. 4 684-93
- [100] Zheng Q et al 2025 Direct synthesis of vinylene-linked conjugated polymers by selective methyl/methylene C—H activation on gold surfaces Angew. Chem., Int. Ed. 64 e202503303
- [101] Emmrich M et al 2015 Subatomic resolution force microscopy reveals internal structure and adsorption sites of small iron clusters Science 348 308–11
- [102] Kawai S *et al* 2016 Superlubricity of graphene nanoribbons on gold surfaces *Science* **351** 957–61

- [103] Huber F, Berwanger J, Polesya S, Mankovsky S, Ebert H and Giessibl F J 2019 Chemical bond formation showing a transition from physisorption to chemisorption *Science* 366 235–8
- [104] Weymouth A J, Riegel E, Gretz O and Giessibl F J 2020 Strumming a single chemical bond *Phys. Rev. Lett.* 124 196101
- [105] Berwanger J, Polesya S, Mankovsky S, Ebert H and Giessibl F J 2020 Atomically resolved chemical reactivity of small Fe clusters *Phys. Rev. Lett.* 124 096001
- [106] Qi J et al 2020 Force-activated isomerization of a single molecule J. Am. Chem. Soc. 142 10673–80
- [107] Liebig A, Hapala P, Weymouth A J and Giessibl F J 2020 Quantifying the evolution of atomic interaction of a complex surface with a functionalized atomic force microscopy tip Sci. Rep. 10 14104
- [108] Barja S et al 2016 Charge density wave order in 1D mirror twin boundaries of single-layer MoSe<sub>2</sub> Nat. Phys.
  12.751–6
- [109] Lantz M A, Hug H J, Hoffmann R, van Schendel P J A, Kappenberger P, Martin S, Baratoff A and Güntherodt H J 2001 Quantitative measurement of short-range chemical bonding forces *Science* 291 2580
- [110] Sugimoto Y, Pou P, Abe M, Jelinek P, Perez R, Morita S and Custance O 2007 Chemical identification of individual surface atoms by atomic force microscopy *Nature* 446 64–67
- [111] Gross L, Mohn F, Liljeroth P, Repp J, Giessibl F J and Meyer G 2009 Measuring the charge state of an adatom with noncontact atomic force microscopy *Science* 324 1428–31
- [112] Mohn F, Gross L, Moll N and Meyer G 2012 Imaging the charge distribution within a single molecule *Nat*. *Nanotechnol.* 7 227–31
- [113] Gross L, Schuler B, Mohn F, Moll N, Pavliček N, Steurer W, Scivetti I, Kotsis K, Persson M and Meyer G 2014 Investigating atomic contrast in atomic force microscopy and Kelvin probe force microscopy on ionic systems using functionalized tips *Phys. Rev. B* 90 155455
- [114] Bartels L, Meyer G and Rieder K H 1999 The evolution of CO adsorption on Cu(111) as studied with bare and CO-functionalized scanning tunneling tips Surf. Sci. 432 L621–L6
- [115] Schneiderbauer M, Emmrich M, Weymouth A J and Giessibl F J 2014 CO tip functionalization inverts atomic force microscopy contrast via short-range electrostatic forces *Phys. Rev. Lett.* 112 166102
- [116] Liu Q, Liu C-X, Xu C, Qi X-L and Zhang S-C 2009 Magnetic impurities on the surface of a topological insulator *Phys. Rev. Lett.* 102 156603
- [117] Potasz P and Fernández-Rossier J 2015 Orbital magnetization of quantum spin Hall insulator nanoparticles Nano Lett. 15 5799–803
- [118] Lühmann T, John R, Wunderlich R, Meijer J and Pezzagna S 2019 Coulomb-driven single defect engineering for scalable qubits and spin sensors in diamond *Nat. Commun.* 10 4956
- [119] Zhang P et al 2025 Synthesis engineering of 2D Co<sub>3</sub>Sn<sub>2</sub>S<sub>2</sub> with tunable anomalous Hall effect Adv. Mater. 37 e09261
- [120] Muechler L, Liu E, Gayles J, Xu Q, Felser C and Sun Y 2020 Emerging chiral edge states from the confinement of a magnetic Weyl semimetal in Co<sub>3</sub>Sn<sub>2</sub>S<sub>2</sub> Phys. Rev. B 101 115106
- [121] Zhang Z, You J-Y, Ma X-Y, Gu B and Su G 2021 Kagome quantum anomalous Hall effect with high Chern number and large band gap *Phys. Rev. B* 103 014410
- [122] Han X *et al* 2025 Atomic manipulation of the emergent quasi-2D superconductivity and pair density wave in a kagome metal *Nat. Nanotechnol.* **20** 1017–25